

AN EXPERIMENTAL INVESTIGATION OF HEAT TRANSFER
TO REUSABLE SURFACE INSULATION TILE ARRAY GAPS IN A TURBULENT
BOUNDARY LAYER WITH PRESSURE GRADIENT

By

David Allen Throckmorton

B.S. in Aerospace Engineering

Virginia Polytechnic Institute

June 1970

A Thesis submitted to

the Faculty of

The School of Engineering and Applied Science

of The George Washington University in partial satisfaction

of the requirements for the degree of Master of Science

February 1975

Thesis directed by

Dr. John L. Whitesides, Jr.

Associate Research Professor of Engineering

N75-14994

JLC:JLB
07570

G3/34

(NASA-CR-141310) AN EXPERIMENTAL
INVESTIGATION OF HEAT TRANSFER TO REUSABLE
SURFACE INSULATION TILE ARRAY GAPS IN A
TURBULENT BOUNDARY LAYER WITH PRESSURE
GRADIENT M.S. Thesis (George Washington



ABSTRACT

An experimental investigation was performed to determine the effect of pressure gradient on the heat transfer to space shuttle reusable surface insulation (RSI) tile array gaps under thick, turbulent boundary layer conditions. Heat transfer and pressure measurements were obtained on a curved array of full-scale simulated RSI tiles in a tunnel wall boundary layer at a nominal freestream Mach number of 10.3 and freestream unit Reynolds numbers of 1.6, 3.3, and 6.1×10^6 per meter. Transverse pressure gradients were induced over the model surface by rotating the curved array with respect to the flow. Definition of the tunnel wall boundary layer flow was obtained by measurement of boundary layer pitot pressure profiles, and flat plate wall pressure and heat transfer.

Flat plate wall heat transfer data were correlated and a method was derived for prediction of smooth, curved array heat transfer in the highly three-dimensional tunnel wall boundary layer flow. Simulation of full-scale space shuttle vehicle pressure gradient levels was assessed. No systematic effect of pressure gradient on RSI tile array gap heat transfer was observed.

ACKNOWLEDGMENTS

The author is indebted to the National Aeronautics and Space Administration for permission to use Space Shuttle program-related research material in this thesis. The author wishes to express his sincere appreciation to Mr. James C. Dunavant of the Langley Research Center for his guidance in the inception of this project, and to Dr. John L. Whitesides for his assistance in the preparation of this thesis. Special thanks are extended to Mrs. Carol M. Forrest for her invaluable assistance in the typing of the several draft versions of the manuscript.

TABLE OF CONTENTS

CHAPTER	PAGE
I. LIST OF FIGURES	v
II. LIST OF SYMBOLS	viii
III. INTRODUCTION	1
IV. EXPERIMENTAL APPARATUS AND PROCEDURES	5
Facility	5
Models and Instrumentation	6
Pressure gradient model	6
Flat plate model	7
Boundary layer probe	8
Test Procedures and Conditions	8
Measurement Techniques	9
Temperature data	9
Pressure data	9
Data Reduction	10
Freestream Flow Quantities	10
Boundary Layer Profiles	10
Heat Transfer Data	11
V. RESULTS AND DISCUSSION	13
Coordinate Definition	13

CHAPTER	PAGE
Boundary Layer Surveys	13
Flat Plate Results	14
Heat transfer data	14
Pressure data	15
Flat plate data correlation	15
RSI Tile Array Results - Smooth Model	17
Pressure data	17
Heat transfer data	18
Prediction of smooth surface heating characteristics	19
RSI Tile Array Results - Gaps Present	23
Pressure data	23
Gap heat transfer data	23
Pressure Gradient Effects on Gap Heat Transfer	26
Shuttle Pressure Gradient Simulation	27
VI. CONCLUDING REMARKS	28
VII. REFERENCES	30
VIII. APPENDIX A	71
IX. APPENDIX B	75

I. LIST OF FIGURES

FIGURE	PAGE
1. Schematic diagram of the facility.	33
2. Langley Continuous Flow Hypersonic Tunnel.	34
3. Model injection mechanism.	35
4. RSI pressure gradient model schematic.	37
5. RSI pressure gradient model.	38
6. RSI pressure gradient model mounted on injection strut . .	39
7. RSI pressure gradient model instrumentation locations. . .	41
8. Flat plate model mounted on injection strut.	42
9. Flat plate model instrumentation locations.	43
10. Boundary layer pitot probe schematic	44
11. Comparison of centerline wall and freestream static pressures.	45
12. Definition of coordinate systems	46
13. Boundary layer velocity profiles at sidewall centerline. $y = 0$	47
14. Transverse variation of boundary layer velocity profile. $Re_m/m = 3.3 \times 10^6$	48
15. Variation of displacement and momentum thicknesses with transverse wall position.	49
16. Heat transfer coefficient distribution on the flat plate..	50
17. Static pressure distribution on the flat plate	51

FIGURE

PAGE

18.	Variation of flat plate Stanton number with momentum thickness Reynolds number	52
19.	Correlation of flat plate heat transfer with displacement thickness	53
20.	Static pressure distributions on the smoothed RSI tile array model	54
21.	Surface heat transfer distributions on the smoothed RSI tile array model	55
22.	Predicted heat transfer to the smoothed RSI tile array model assuming modified Newtonian pressure. $Re_{\infty}/m = 3.3 \times 10^6$	58
23.	Comparison of measured and modified Newtonian pressures on the smoothed RSI tile array model. $Re_{\infty}/m = 3.3 \times 10^6$	59
24.	Comparison of measured and predicted heat transfer to the smoothed RSI tile array model using measured pressure data. $Re_{\infty}/m = 3.3 \times 10^6$	60
25.	Static pressure distributions on the RSI tile array model	61
26.	Distribution of heat transfer within the transverse gap. $Re_{\infty}/m = 3.3 \times 10^6$	62
27.	Variation of heat transfer to the streamwise gap with array rotation angle. $Re_{\infty}/m = 3.3 \times 10^6$	65
28.	Variation of heat transfer to the transverse gap with array rotation angle. $Re_{\infty}/m = 3.3 \times 10^6$	67

FIGURE

PAGE

29. Variation with array rotation angle of heat transfer to the transverse gap at its intersection with the stream-wise gap. $Re_{\infty}/m = 3.3 \times 10^6$ 68
30. Effect of pressure gradient on heat transfer to the transverse gap 69
31. Full scale vehicle pressure gradient simulation.
 $M_{\infty} = 10.0, \bar{\alpha} = 30^{\circ}$ 70

II. LIST OF SYMBOLS

A	constant in Equation (8)
B	constant in Equation (8)
c_p	constant pressure specific heat of air, j/kg-K
c_{p_m}	specific heat of model material, j/kg-K
d	gap depth, cm
h	heat transfer coefficient, W/m ² -K
k	constant in Equation (15)
L	full-scale tile dimension, cm
M	Mach number
N_{St}	Stanton number, $\equiv \frac{h}{\rho_w u_e c_p}$
P	pressure, N/m ²
P_{t_2}	total pressure behind a normal shock in the freestream, N/m ²
q	heat transfer rate, W/m ²
R	universal gas constant, m ² /sec ² -K
R_{surf}	radius of curved array model, cm
r	recovery factor
$Re_{w,\theta}$	Reynolds number based on wall conditions and boundary layer momentum thickness, $\equiv \frac{\rho_w u_e \theta}{\mu_e}$
Re_∞/m	freestream unit Reynolds number, $\equiv \frac{\rho_\infty u_\infty}{\mu_\infty}$, 1/m
S	surface dimension defined in figure 31, m
T	temperature, °K
t	time, sec
u	velocity, m/sec
W	tunnel test section half-width, cm

w	gap width, cm
X, Y, Z	coordinates defined in figure 12
x, y, z	coordinates defined in figure 12
Y_{\max}	maximum vehicle planform dimension defined in figure 31, m
y_{surf}	y-dimension of local curved model surface, cm
z_{surf}	z-dimension of local curved model surface, cm
α	array rotation angle, degrees
$\bar{\alpha}$	angle of attack, degrees
δ^*	boundary layer displacement thickness, cm
δ_{eff}^*	"effective" boundary layer displacement thickness defined in Equation (15), cm
θ	boundary layer momentum thickness, cm
ϕ	angle between surface tangent plane and flow velocity vector, degrees
λ	model material thickness, m
ρ	density of air, kg/m ³
ρ_m	model material density, kg/m ³
μ	viscosity, N-sec/m ²

Subscripts:

aw	adiabatic wall
e	boundary layer edge
fp	flat plate
sm	surface of the smooth, curved array
t	total
w	wall
∞	freestream

III. INTRODUCTION

The space shuttle orbiter is being designed for an operational life in excess of 100 reentry missions with minimal required refurbishment between those missions. In order to meet this requirement, the vehicle thermal protection system (TPS) will be a surface covering of a non-metallic, low-density refractory oxide. This material, referred to as Reusable Surface Insulation (RSI), is capable of withstanding without degradation repeated exposure to the harsh reentry environment, while insulating the cold structure of the vehicle from surface temperatures in excess of 1500° K. The material will be attached to the vehicle surface in a "brick-like" array of square tiles (15.24 x 15.24 cm) which vary in thickness from approximately 1-10 centimeters according to the intensity of the local heating environment. Small gaps between tiles will allow for thermal expansion of the tile material. Interference heat transfer to the tile exterior and gap wall surfaces is of major concern to the TPS designer. The presence of the gaps may result in increased boundary-layer turbulence and attendant increased surface heating. Heating levels within the gaps, which would be expected to be substantially lower than surface values, may be similarly severe due to flow reattachment phenomena. In addition, radiation blockage within the gaps may produce extreme temperatures even at low heating levels, and the shortened heat paths may result in excessive bond-line temperatures.

Effective design of the TPS requires a sound knowledge of the aerodynamic heating environment to which the RSI tiles will be subjected. This knowledge must include an accurate definition of the heat transfer distribution about a tile and a good understanding of how this distribution is affected by boundary layer state (laminar/turbulent), boundary layer thickness, flow angularity, gap width, tile edge radius, tile stacking arrangement, and other parameters.

Present day understanding of heat transfer in gap or cavity flows has resulted from past studies of the general problem of heat transfer in regions of separated flow. Chapman (ref. 1) attacked the problem of a purely laminar separated flow region theoretically. His analysis, which assumed a boundary layer of zero thickness at the separation point, predicted that the average heating to the separated region was only 56 percent of that for attached flow under similar conditions. Chapman's theory was not capable of predicting heat transfer distributions. Larson (ref. 2) experimentally verified Chapman's result and found a similar reduction in average heat transfer of about 60 percent for separated turbulent boundary layers.

Charwat, et al (refs. 3 and 4) made extensive measurements of the pressure and heat transfer distributions in cavities under turbulent boundary layer conditions at subsonic and low supersonic Mach numbers. They were able to identify a critical cavity width-to-depth ratio which "separates" the cavity flow into two distinct types. When this width-to-depth ratio is exceeded, the flow separates at the forward

cavity wall and reattaches to the cavity floor as a rear-facing step, then separates again ahead of the upstream-facing cavity wall. This type of flow is termed "closed" cavity flow. When the width-to-depth ratio falls below the critical value, the boundary flow bridges the cavity entirely, reattaching at the upstream-facing wall, and is termed "open" cavity flow. Additional experimental studies of cavity-type separated flows are reported in refs. 5-10 for the laminar case and refs. 11-15 for the turbulent case.

Burgraff (ref. 16) approached the gap heating problem analytically for the laminar separation condition. His analysis postulated an inviscid recirculating core flow within the cavity, and, therefore, is not applicable to fully viscous cavity flows. Nestler (ref. 17 and 18) approached the problem for both laminar and turbulent cases by analyzing the shear layer development and reattachment, assuming a wall jet heating decay from the reattachment point.

The gap heating problem for shuttle is one which will occur in deep gaps where the ratio of gap width-to-depth (w/d) is less than 0.08. (Gap width will be nominally $\sim .082$ cm.) Typically, the gap heating environment for shuttle will consist of an oncoming boundary layer with thickness far in excess of the local gap width ($\delta^*/w \gg 1$). All of the investigations previously mentioned, however, have dealt with cavities with width-to-depth ratios much greater than the shuttle value (usually > 1), and boundary layer thicknesses generally much less than the gap width. Only the data of Weiting (ref. 9) for laminar flow, begin to

approach the gap and boundary layer geometries of interest for the shuttle.

In support of the space shuttle technology program, an experimental effort has been focused on the shuttle-related gap heating problems. Evaluation of TPS tile material thermal performance (ref. 19) and definition of the gap heating environment are important elements in this effort. Johnson (ref. 20) studied the effects of gap width and boundary layer thickness on TPS gap heating for turbulent flow over a simulated tile array at Mach 8. This work revealed a potential heating problem area at the intersection of streamwise and transverse running gaps. Throckmorton (ref. 21) obtained data on a simulated tile array in a turbulent boundary layer to investigate the effects of gap width, flow angularity, and tile surface mismatch on tile gap heating. Foster et al (ref. 22) investigated the effect of similar parameters for single gaps and gap intersections in laminar flow. A compilation and analysis of these and other recent gap heating data may be found in ref. 23.

Because of entry angles of attack and the complex curvatures of the orbiter external surface, boundary layer flows over much of the flight vehicle will be strongly influenced by gradients in surface pressure. Each of the recent studies of TPS gap heating phenomena, however, have been conducted on sharp flat plates or in tunnel wall boundary layers under conditions of zero pressure gradient. The present investigation was undertaken to assess possible effects of pressure gradient on the heat transfer to RSI tile array gaps under thick, turbulent boundary layer conditions.

IV. EXPERIMENTAL APPARATUS AND PROCEDURES

Heat transfer and pressure measurement tests were made on a curved array of full-scale simulated RSI tiles submerged in a thick, turbulent, tunnel-sidewall boundary layer. Transverse pressure gradients of varying magnitude were induced over the model surface by rotating the curved array with respect to the flow direction. This enabled the study of RSI tile array gap heating as affected by pressure gradient. The tile array was tested both with gaps present, and with the gaps filled and smoothed to provide smooth-surface reference data.

Heat transfer and pressure measurements were also made on a smooth flat plate mounted in the tunnel sidewall. These data, along with measured pitot pressure profiles, provided a definition of the characteristics of the 3-dimensional boundary layer flow in which tile array tests were conducted.

Facility

The experimental results presented herein were obtained in the Langley Research Center Continuous Flow Hypersonic Tunnel. This facility, which has a 78.74 cm (31-inch) square test section, operates at a nominal freestream Mach number of 10.3 over a freestream unit Reynolds number range of $1.5 - 8.2 \times 10^6$ per meter using air as the test gas. The tunnel may be operated in either a blowdown or continuous, closed-circuit mode. A schematic of the tunnel circuit is shown in figure 1. For continuous operation, the high pressure air supply and vacuum sphere are used to initiate the hypersonic flow. When the flow has been

established, the second minimum is closed down, and the compressors brought into the loop to maintain the hypersonic flow. Air heaters are of the tubular, electrical resistance type. The tunnel throat, expansion, and diffuser sections are all water cooled. A photograph of the facility is presented in figure 2.

For these tests, the models were mounted on the model injection mechanism which is shown adjacent to the test section in figure 3. This device allows a model to be isolated from the hypersonic airstream for model cooling or geometric changes. The mechanism also provides rapid injection of a model into the hypersonic airstream.

Models and Instrumentation

Pressure gradient model.- The RSI tile pressure gradient model was a curved array of simulated full-scale RSI tiles fabricated of Inconel sheet with a nominal thickness of 0.0483 cm. Surface curvature was defined by a right circular cylinder of 102.28 cm radius, cut by a plane at a 5 degree angle to the axis of the cylinder. A model schematic is shown in figure 4. Individual tile size was 14.92 cm square.

The model was fabricated such that each transverse row of simulated tiles was a continuous sheet of material with the streamwise gaps formed by bending. The transverse gaps were fabricated separately and electron beam welded between tile row sections to form the complete tile array. Stress relief in the material following the welding process resulted in a "pinching down" of the transverse gaps from the desired width. Resulting gap width between tiles was nominally 0.30 cm

for streamwise running gaps and 0.20 cm for transverse gaps. Gap depth was 2.86 cm. A photograph of the model is shown in figure 5.

Spacer plates were also fabricated to maintain model edges flush with the tunnel sidewall. Three sets of spacer plates were fabricated to allow testing at model flow angularities of 0, ± 22.5 , and ± 45 degrees. The model and spacer plates mounted on the facility injection system for testing are shown in figure 6.

The model was instrumented with 67 chromel-alumel thermocouples spot-welded to the model back-surface at tile surface and gap locations defined in figure 7. The model was also fitted with 12 static pressure orifices located as shown in figure 7.

For smooth surface testing of the model, the gaps were eliminated by filling them with twine to a point approximately one gap width below the tile exterior surface. The remainder of the gap was filled with plaster of paris which was allowed to dry and then smoothed by sanding to match the surrounding surface. This created a smooth model with correct curvature for measurement of surface reference data.

Flat plate model.— The smooth flat plate model, used to measure undisturbed wall heat transfer coefficient, was fabricated from 321 stainless steel sheet with a nominal thickness of 0.127 cm. The 50.8 cm square panel fit flush with the injection plate fabricated for testing of this model. The model and injection plate are shown mounted on the injection strut, ready for testing, in figure 8. The flat plate model was instrumented with 11 chromel-alumel thermocouples spot-welded to the model back-surface, located as shown in figure 9.

Boundary-layer probe.- A boundary-layer rake with 11 pitot probes was fabricated for use with the flat plate model. The rake could be placed downstream of the flat plate model at four spanwise locations. Individual pitot probes were located at stations normal to the wall as shown in the rake schematic of figure 10. Tube diameters varied with position relative to the wall. The rake is shown installed with the flat plate model for testing in figure 8.

Test Procedures and Conditions

The transient calorimeter technique was used to measure the heat transfer rates to the surfaces of the thin skin models. The tests were conducted with the models initially at room temperature, isolated from the hypersonic airstream within the injection chamber, at a pressure equal to the test section static pressure. With the hypersonic flow established in the test section, the model was rapidly injected to the test position, flush with the tunnel sidewall, and data were automatically recorded at a rate of 20 samples/second. After the model had been exposed to the airstream for an interval of time sufficient to allow pressure transducer outputs to "settle out," the model was retracted from the stream into the injection box.

Both the tile array and flat plate reference models were tested at nominal freestream total pressures of 2.41, 5.17, and 9.65×10^6 N/m²; corresponding to freestream unit Reynolds numbers of 1.6, 3.3, and 6.1×10^6 per meter. The tile array model was tested at flow angles, α , of 0, $\pm 22.5^\circ$, and $\pm 45^\circ$. Testing at positive and negative

flow angles allowed measurement of both temperature and pressure data over the entire model surface while instrumenting only one side of the plane of symmetry for either temperature or pressure as shown in figure 7. By "mirror imaging" the data obtained at negative flow angles, data for the entire model surface was obtained for flow angles of $\alpha = 0^\circ$, 22.5° , and 45° .

Measurement Techniques

Temperature data.- Temperature data were obtained using the chromel-alumel thermocouples with a reference junction of 324.8 K. The reference junction temperature was thermostatically controlled to within $\pm 0.55^\circ$ K. Freestream total temperature was measured at the centerline of the tunnel settling chamber immediately upstream of the nozzle.

Pressure data.- Freestream total pressure was measured in the settling chamber by three strain-gage-type transducers. The transducers had ranges of 0-3.45, 0-6.89, and 0-17.24 $\times 10^6$ N/m². The transducer with the lowest pressure range which remained on scale was used to record the data.

Static pressures were measured using baratrons mounted on the injection strut immediately behind the model. The baratron is a capacitance-type transducer, operated in conjunction with a signal conditioner to allow measurement of pressure over seven ranges from 0-68.9 N/m² through 0-6.89 $\times 10^4$ N/m². The signal conditioner provides automatic ranging such that the measurements were obtained on the lowest possible range.

Data Reduction

Freestream Flow Quantities.- Freestream Mach number was determined from previously obtained tunnel flow calibrations. Freestream temperature and pressure quantities were calculated using the one-dimensional perfect gas relations of ref. 24 with corrections for real gas imperfections. The real gas correction factors were derived from the work of Erickson and Creekmore (ref. 25) on thermodynamic properties of equilibrium air. Fluid viscosity was calculated using the Sutherland relation for low temperature, shown below in SI units:

$$\mu = 1.458 \times 10^{-6} \frac{T^{3/2}}{T + 98.33} \frac{\text{N-sec}}{\text{m}^2}, T \sim ^\circ\text{K} \quad (1)$$

Boundary Layer Profiles.- Boundary layer velocity and density profiles were derived from flat plate wall boundary layer pitot pressure measurements. These calculations required assumptions of the distribution of static pressure and temperature through the boundary layer. As shown in figure 11, the measured flat plate static pressure was significantly higher than the computed freestream static pressure. Static pressure within the boundary layer was assumed to vary linearly between the measured wall and computed freestream values.

Total temperature within the boundary layer was assumed to vary as the square of velocity,

$$\frac{T_t - T_w}{T_{te} - T_w} = \left[\frac{u}{u_e} \right]^2 \quad (2)$$

which is characteristic of turbulent nozzle-wall boundary layers (ref. 26). Unpublished total temperature measurements made by D. H. Crawford in the wall boundary layer of this facility show good agreement with the quadratic temperature-velocity relation.

With the measured pitot pressure and assumed static pressure at each point, the Raleigh pitot equation was applied to calculate local Mach number. Local velocity and density were then computed using the assumed temperature distribution and the perfect gas equation of state.

Heat Transfer Data.— The test procedure of rapid injection of the isothermal model to the test position provided a step input in heat transfer to the thin-skin model. Heat transfer rates were determined by the transient-calorimeter technique of measuring the time-rate-of-change of the model skin temperature.¹ For data reduction purposes, the one-half second interval of temperature data immediately following model injection was disregarded to allow steady-state conditions to stabilize in the gap flow. This time is in excess of the required time as reported by Nicoll, ref. 27. A quadratic least squares curve was fit to the subsequent 4-second interval of data for each thermocouple. Rates-of-change of temperature with time ($\partial T_w / \partial t$) were evaluated analytically from the curve fit expressions at the initial point of each curve fit.

¹ A detailed assessment of the accuracy of this technique for these tests is contained in Appendix A.

Heat transfer rates were then computed from the expression

$$q = \rho_m c_{p_m} \lambda (\partial T_w / \partial t) \quad (3)$$

Heat transfer data are expressed in the form of the heat transfer coefficient (h) defined as

$$h = \frac{q}{T_{aw} - T_w} \quad (4)$$

Adiabatic wall temperature (T_{aw}) was computed from the relation

$$r = \frac{T_{aw} - T_\infty}{T_t - T_\infty} \quad (5)$$

where recovery factor (r) was assumed equal to 0.89.

V. RESULTS AND DISCUSSION

Coordinate Definition

In the discussion of experimental results which follows, the data are referenced to coordinate systems defined in figure 12. All flat plate and wall boundary layer data are referenced to a stream-oriented coordinate system (X, Y, Z) which is fixed within the flow. All curved panel data, both smooth and with gaps present, are referenced to a coordinate system (x, y, z) fixed within the rotating curved array. The origins of both coordinate systems are located on the tunnel sidewall at the center of rotation of the tile array model.

Boundary Layer Surveys

Boundary layer velocity profiles measured on the sidewall centerline are presented in figure 13 for the four freestream unit Reynolds numbers at which flat plate data were obtained. The profile shapes are characteristic of a fully developed turbulent boundary layer and the profiles tend to "fill-out" (boundary layer thins) with increasing unit Reynolds number. Profiles obtained at several transverse locations at a single unit Reynolds number are compared in figure 14. A significant change in the boundary layer profile shape as a function of transverse position is observed. This transverse variation in boundary layer profile is an indication of the 3-dimensional character of the boundary layer flow in a nozzle of square cross-section. Although they do not present all of the measured profile data, figures 13 and 14 illustrate

the trends observed in the data for the unit Reynolds numbers and transverse locations at which profiles were measured.

In order to more readily define the effects of freestream unit Reynolds number and transverse location on boundary layer characteristics, the measured profile data were integrated to obtain values of the bulk quantities of boundary layer displacement (δ^*) and momentum (θ) thicknesses. The quantities are defined by the relations

$$\delta^* = \int_0^{\infty} \left(1 - \frac{\rho u}{\rho_e u_e}\right) dz \quad (6)$$

$$\theta = \int_0^{\infty} \left(1 - \frac{u}{u_e}\right) \frac{\rho u}{\rho_e u_e} dz \quad (7)$$

and are a measure of the mass flow and momentum flux deficits respectively, within the boundary layer. The variations of these quantities with freestream unit Reynolds number and transverse position are presented in figure 15. Momentum thickness decreases, as expected, with increasing unit Reynolds number and shows little transverse variation. Boundary layer displacement thickness does not change significantly with unit Reynolds number. Displacement thickness does, however, decrease rapidly with transverse position, reflecting the changes in boundary layer profile shape noted in figure 14.

Flat Plate Results

Heat transfer data.— Measured flat plate heat transfer coefficients are shown in figure 16 for the full range of test conditions. At each

total pressure, the heat transfer increases in the transverse direction, primarily as a result of the thinning of the boundary layer, and is symmetric about the centerline. The streamwise distribution of heat transfer exhibits a heating decay characteristic of a fully-developed thickening boundary layer.

Pressure data.- The flat plate pressure data (figure 17) show a transverse distribution similar to that of the heat transfer data. Streamwise, however, the pressure decreases to a minimum and increases in the downstream (+X) direction. This behavior is attributed to the fact that the test section area of this facility does not represent a complete expansion of the flow from the tunnel throat. The tunnel nozzle expands the flow to a point, approximately one meter upstream of the test section center, at which the flat, parallel walls of the test section begin. The intersection of the expansion section and test section walls then constitutes a compression corner for the wall boundary layer flow. The data presented herein were obtained in the compression region downstream of this corner.

Flat plate data correlation.- As a basis for understanding the mechanisms controlling the flat plate wall boundary layer heat transfer, the heating data of figure 16 were correlated with parameters which could be expected to influence heat transfer. Figure 18 presents flat plate heating data expressed in the form of Stanton number, N_{St} , plotted as a function of Reynolds number based on wall conditions and boundary layer momentum thickness, $Re_{w,\theta}$. The heat transfer data points were

inferred from the data of figure 16 for the transverse locations at which boundary layer profiles were obtained.

At each transverse location, Stanton number and Reynolds number correlate the data over the range of freestream flow conditions. This result is not unexpected, since for fully developed turbulent boundary layers over flat plates, heat transfer over a Reynolds number re can normally be correlated by Stanton and Reynolds numbers (ref.).

For this tunnel wall boundary layer flow, Stanton number was found to vary as the wall Reynolds number, $Re_{w,0}$, to the $-.07$ power at each transverse location, as indicated in figure 18. Failure to correlate the data for the three transverse locations is not surprising, as the Stanton/Reynolds number correlation relates changes in streamwise variables and has no application to transverse flow phenomena. The upstream histories of the boundary layers affecting each transverse location are unique and no simple boundary layer parameter relates the transverse influence of boundary layer characteristics. The single parameter which varies significantly in the transverse plane is boundary layer displacement thickness; and for a given boundary layer flow, heat transfer is known to decrease with increasing boundary layer thickness. As previously noted, for this tunnel wall flow, displacement thickness does not vary significantly with unit Reynolds number. The effect of transverse boundary layer thickness variation on tunnel sidewall heat transfer is indicated in figure 19 where the data of figure 18 are presented as a function of displacement thickness. The flat plate heat transfer data correlate with pertinent flow variables according to the

relation

$$N_{St} Re_{w,\theta}^{.07} = A \frac{\delta^*}{W} + B$$

where W is defined as the tunnel test section half-width (39.37 cm).

$$A = -0.0109$$

$$B = 0.00466$$

RSI Tile Array Results - Smooth Model

Because of the complexity of the wall boundary layer flow indicated by the flat plate and boundary layer probe results, heat transfer and pressure data were obtained on the RSI tile array model with no gaps present. The data were used to relate measured surface and gap heating to an undisturbed surface reference.

Pressure data.- Smooth model pressure data and fourth-order least squares curve fits of the data are presented in figure 20 for all test conditions. The data from the orifice located at $y = \pm 5.08$ cm were not considered for computation of the curve fit expressions as data from this transducer were consistently higher than that from the other transducers. At an array rotation angle, α , of 0° , the pressures show the same transverse trends demonstrated by the flat plate data. Flow deflection angle, ϕ (i.e. the angle between the freestream velocity vector and the plane of tangency of the surface at a point), has negligible point to point variation between orifices when $\alpha = 0^\circ$. With increases in rotation angle, α , to 22.5° and 45° , flow deflection angles on the

upstream portion of the model increase, those on the downstream portion decrease, and static pressures vary accordingly.¹

Heat transfer data.- Measured smooth surface reference heat transfer data are presented in figure 21. For the zero rotation angle case, heat transfer increases, as expected, with transverse distance from the centerline. The rate of increase, however, is greater than that measured for the flat plate. This more rapid increase is hypothesized to be the result of an effective "thinning" of the boundary layer due to the protrusion of the model into the boundary layer flow. With a boundary layer which is much thicker than the protruding height of the tile array model, it is not thought that the model will significantly affect the outer portions of the boundary layer as would be the case if the characteristic dimension of the model was of the same order as the boundary layer thickness. Rather, the boundary layer edge location remains essentially unchanged from the flat plate case and the boundary layer thickness is decreased by the protrusion of the curved model into the flow.

¹Note that the y-coordinate is fixed in the rotating array, while the Y-coordinate is fixed in the tunnel sidewall. While y-values are constant for each orifice, the orifice locations within the complex boundary layer flow vary with array rotation angle. Therefore, the pressure and heat transfer variations shown in the figures as functions of the y-coordinate, are a superposition of effects of changing flow deflection angle, and changes in Y-coordinate position (boundary layer conditions affecting the point). Derivation of the expression for flow deflection angle as a function of y-location and array rotation angle, α , is contained in Appendix B.

Smooth surface heating data for the $\alpha = 22.5^\circ$ and 45° cases show increased surface heating with increasing flow deflection angle (y-increasing) as expected. The data also show, however, increases in heating where the flow deflection angle is decreasing (y-decreasing). This anomaly is explained by the fact that these heating increases, in regions of decreasing flow deflection, are occurring at wall positions where boundary layer thickness is decreasing. The opposing effects of decreasing boundary layer thickness and flow deflection angle are dominated by the boundary layer thinning effect, and heating increases. In the following section, a method will be developed to predict smooth model surface heat transfer. This prediction method uses the measured flat plate heat transfer and pressure data as a base and perturbs these data to account for the flow deflection and boundary layer thinning effects which result from curved panel rotation.

Prediction of smooth surface heating characteristics.— Consider the correlation of flat plate heating data presented in figure 19:

$$N_{St} Re_{w,\theta}^{.07} = A \frac{\delta^*}{W} + B \quad (8)$$

and assume that a correlation of this form is valid for the smooth curved panel data. Therefore, for curved panel data:

$$\frac{N_{St} Re_{w,\theta}^{.07}}{(N_{St} Re_{w,\theta}^{.07})_{fp}} = \frac{A \frac{\delta_{eff}^*}{W} + B}{(A \frac{\delta^*}{W} + B)_{fp}} \quad (9)$$

where δ_{eff}^* is an effective boundary layer thickness as hypothesized in the previous section. By definition,

$$N_{\text{St}} \equiv \frac{h}{\rho_w u_{\infty} c_p} \quad \text{and} \quad \text{Re}_{w,\theta} \equiv \frac{\rho_w u_{\infty} \theta}{\mu_w}$$

Substituting these expressions in Equation (9),

$$\left[\frac{\left(\frac{h}{\rho_w} \right)}{\left(\frac{h}{\rho_w} \right)_{fp}} \right] \left[\frac{\left(\frac{\rho_w \theta}{\mu_w} \right)}{\left(\frac{\rho_w \theta}{\mu_w} \right)_{fp}} \right]^{0.07} = \frac{A \frac{\delta_{\text{eff}}^*}{W} + B}{(A \frac{\delta_{\text{eff}}^*}{W} + B)_{fp}} \quad (10)$$

Assuming a perfect gas,

$$\rho = \frac{P}{RT} \quad (11)$$

and assuming wall temperature fluctuations are negligible,

$$T_w \approx (T_w)_{fp} \quad \text{and} \quad \mu_w \approx (\mu_w)_{fp}$$

then,

$$\left[\frac{\left(\frac{h}{P} \right)}{\left(\frac{h}{P} \right)_{fp}} \right] \left[\frac{\frac{P\theta}{(P\theta)_{fp}}}{\left(\frac{P\theta}{(P\theta)_{fp}} \right)} \right]^{0.07} = \frac{A \frac{\delta_{\text{eff}}^*}{W} + B}{(A \frac{\delta_{\text{eff}}^*}{W} + B)_{fp}} \quad (12)$$

Neglecting the weak dependence on θ :

$$\frac{h}{h_{fp}} = \left(\frac{P}{P_{fp}} \right)^{0.93} \frac{A \frac{\delta_{eff}^*}{W} + B}{(A \frac{\delta_{eff}^*}{W} + B)_{fp}} \quad (13)$$

For the purpose of demonstrating the predicted distribution of heat transfer to all tiles in the model array, an estimate of the local pressure level must be made. Modified Newtonian Theory is applied to estimate the wall static pressure variation as affected by transverse location and flow deflection angle. The Modified Newtonian expression for pressure, referenced to the flat plate value ($\phi = 0$) is:

$$\frac{P}{P_{fp}} = 1 + \left(\frac{P_{t2}}{P_{fp}} - 1 \right) \cos^2 (90 + \phi) \quad (14)$$

Now estimate

$$\delta_{eff}^* = \delta^* - k z_{surf} \quad (15)$$

where z_{surf} is the local protrusion of the smooth model surface into the boundary layer flow and k is a constant. The value of the constant, k , which provided a "best fit" to the experimental data was found to be 0.5.

By applying the known flat plate pressure, heat transfer, and boundary layer information to expressions (15), (14), and (13), the distribution of heating to the surface of the smooth, curved panel may

be predicted for all flow conditions and panel rotation angles. Predicted heat transfer distributions for the smooth model at a freestream Reynolds number of 3.3×10^6 per meter and array rotation angles of 0° , 22.5° , and 45° are shown in figure 22. Comparison of the theory of figure 22 with the corresponding data of figure 21 demonstrates that the prediction of transverse heating trends by Equation (13) is good. The failure of the theory to more accurately predict heating level is attributed to the inaccuracy of the modified Newtonian pressure predictions.

A comparison is made in figure 23 of the measured and predicted smooth panel pressures. The failure of the modified Newtonian method to more accurately predict pressure level was not unexpected as this method is applicable to hypersonic flows of uniform total pressure. In this case, the method was applied to a boundary layer, a flow of non-uniform total pressure, without consideration of the total pressure variation within the boundary layer. The intention here, however, was to reproduce trends in pressure level, not necessarily magnitude; and the modified Newtonian approach did this satisfactorily.

If the actual local pressure level were known, it then appears that the local heat transfer could be predicted reasonably well using this approach. Figure 24 presents measured heat transfer data for the transverse ray along which pressure data were also measured for the 3.3×10^6 /m Reynolds number case. The predicted heating from Equation (13), using the measured pressure data, shows excellent agreement with the measured heat transfer. Similar results were observed in the data obtained at Reynolds numbers of 1.6 and 6.1×10^6 per meter.

RSI Tile Array Results - Gaps Present

Pressure data.- Measured pressures for the simulated RSI tile array are presented in figure 25 for all test conditions. Tile surface data are shown as open symbols, gap floor data as solid symbols. Comparison of these data with that of figure 20 indicates that the surface pressure distributions with gaps present are essentially identical to those obtained with a smooth model. Pressure level within the gaps closely follows that of the tile exterior surface.

Gap heat transfer data.- Measured distributions of heat transfer¹ along the instrumented transverse gap are shown in figure 26 for each array rotation angle at the 3.3×10^6 /m Reynolds number flow condition. For the zero rotation case (figure 26(a)), at a transverse position off the centerline, the surface flow completely bridges the gap with no intense reattachment heating occurring at the gap corner, nor any significant change in surface heating downstream of the gap. Note also that off the centerline at a depth into the gap of less than four gap widths (Δ -symbol), the local heating level is less than 2 percent of the undisturbed surface value. The solid symbols of figure 26, and those figures to follow, indicate heat transfer data which are of questionable accuracy. The model skin temperature increases from which these data were derived were of the same order as the precision of the measurement apparatus. The heat transfer rates which resulted from the temperature

¹All heat transfer data discussed in this section are non-dimensionalized by the measured heat transfer to the smooth surface model. Surface data are normalized by the smooth model measurement of the same thermocouple; gap wall data are normalized by the smooth model surface measurement at the thermocouple location nearest the gap.

data curve fits are then affected as much by recording system data scatter as by steady state convective heating. These data are included for completeness.

For the zero rotation case, figure 26(a), on the array centerline ($y = 0$), the gap geometry consists of a streamwise gap intersecting the transverse gap, creating a stagnation region on the transverse gap wall at the intersection point. Heat transfer within the gap at the intersection point is significantly higher than that for a simple transverse gap as exists away from the centerline. This heating increase at the gap intersection is attributed to impingement of the "channel" flow in the streamwise gap upon the forward-facing wall of the transverse gap. Excessive heating at such gap intersections poses a serious problem for the shuttle TPS designer. Dunavant and Throckmorton (ref. 29), using gap intersection data from several facilities, have shown that such data may be correlated as a function of boundary layer displacement thickness, streamwise gap running length, gap width, and gap depth location.

Rotation of the tile array, figures 26(b-c), produces slight increases in the surface reattachment heating, as effective gap width increases with rotation, and negligible changes in the heating levels within the gap. The only significant change in the gap heating distribution is a transverse shift of the heating peak within the gap which results from the gap intersection phenomena, as array rotation angle increases. Results obtained at Reynolds number of 1.6 and $6.1 \times 10^6/\text{m}$ are similar to those shown.

Figure 27 presents heat transfer data for the streamwise gap at a Reynolds number of $3.3 \times 10^6/m$ as a function of array rotation angle. The significant variations in gap heating observed in these plots result from the transition of the wall from one which is upstream-facing to one which is downstream-facing as array rotation angle changes. When the wall is downstream-facing ($\alpha > 0$), the flow appears to separate upstream of the corner thermocouple, resulting in heating lower than the undisturbed surface value. When the wall is upstream-facing ($\alpha < 0$), the flow reattaches in the vicinity of the corner thermocouple resulting in heating equivalent to or greater than the undisturbed surface value. This result is in opposition to that observed in figure 26(c), ($y = 3.81$ cm), where the flow appeared to completely bridge the gap, attaching downstream of the corner. These contrasting results are attributed to differences in the gap width and corner radii between the streamwise and transverse gaps. As a result of the model fabrication process discussed previously, streamwise gap width was approximately 1.5 times as large as transverse gap width and streamwise gap edge radius was significantly larger than that of the transverse gap. The increased gap width and large exposed surface area at the streamwise gap edge allow for diffusion of the shear layer into the gap and flow reattachment at the tile corner as opposed to the "bridging" phenomena observed for the transverse gap.

The variations of gap heat transfer with rotation angle for the simple transverse gap, and the gap intersection, are presented in

figures 28 and 29, respectively, for the $3.3 \times 10^6/m$ Reynolds number case. Array rotation angle has negligible effect upon the heating to the simple transverse gap (figure 28). However, for the gap intersection location (figure 29), array rotation tends to increase the local heating near the tile surface while resulting in decreased heating at depth within the gap. Again, data at other unit Reynolds numbers demonstrate similar trends.

Pressure Gradient Effects on Gap Heat Transfer

The discussion of the previous section has centered upon the effects of array rotation on the heat transfer within the gap. Rotation of the curved array not only produced crossflow over the array, but also the desired pressure gradient within the gap, providing for determination of the effect of pressure gradient upon heat transfer within the gap. The magnitude of this pressure gradient was determined by differentiating the curve fits of the gap pressure data of figure 25.

In figure 30, measured heat transfer in the transverse gap at $y = \pm 3.81$ and ± 11.43 cm is presented as a function of a non-dimensional pressure gradient parameter. This parameter, $(\partial P / \partial y) (L/P)$, is the local pressure gradient divided by the local pressure times some characteristic length. Using the full-scale tile dimension as the characteristic length ($L = 15.24$ cm), this parameter is physically a $\Delta P/P$ parameter for one tile length along the gap. No systematic effect of pressure gradient on gap heat transfer is evident.

Shuttle Pressure Gradient Simulation

In order to evaluate the full-scale shuttle pressure gradient simulation obtained with the curved array model, full-scale vehicle spanwise pressure distributions were obtained at two longitudinal stations. These pressure distributions were calculated for a full-scale vehicle at Mach 10.0 and 30° angle of attack in a real gas. The surface pressure distributions were numerically differentiated to obtain the full-scale values of the pressure gradient parameter, $(\partial P / \partial S) (L/P)$. Values of this parameter for the full-scale vehicle, are presented in figure 31 as a function of surface dimension, S/Y_{\max} , for the two longitudinal stations illustrated. The shaded area superimposed upon these data indicates the range of pressure gradient parameter values obtained in the wind-tunnel tests. Simulation of full-scale vehicle pressure gradient levels is excellent with the exception of the wing leading edge regions. Wing leading edge TPS, however, will be a solid material with no gaps present. Therefore, the effect of pressure gradient on gap heating is not of concern on that portion of the vehicle surface.

VI. CONCLUDING REMARKS

An experimental investigation has been undertaken to assess the effect of pressure gradient on the heat transfer to reusable surface insulation (RSI) tile array gaps submerged in a thick, turbulent boundary layer. The experimental program consisted of heat transfer and pressure measurements on a curved array of full-scale simulated RSI tiles in the tunnel wall boundary layer of the Langley Research Center Continuous Flow Hypersonic Tunnel over a range of freestream Reynolds numbers and flow angularities. The tile array model was tested with gaps present, and with gaps eliminated to obtain smooth surface reference data. In order to gain a thorough understanding of the boundary layer flow in which these tests were conducted, measurements of tunnel wall boundary layer pitot profiles and flat plate wall pressure and heat transfer were also made.

The measured flat plate wall heat transfer data were correlated with measured boundary layer parameters and a method was developed for prediction of smooth, curved array surface heat transfer. An assessment was made of the full-scale vehicle pressure gradient simulation.

The results of this investigation indicate the following:

(1) The wall boundary layer in the square test section of the Langley Research Center Continuous Flow Hypersonic Tunnel is highly three-dimensional with significant transverse thickness variations.

(2) Heat transfer to the tunnel wall correlates with momentum thickness Reynolds number and boundary layer displacement thickness.

(3) Heating to the curved tile array in this flow was more sensitive to transverse position than was the flat plate data. This sensitivity resulted from thinning of the boundary layer by the protrusion of the curved array surface into the flow.

(4) A method has been derived for prediction of smooth, curved array heat transfer in this tunnel wall boundary layer flow. The method uses predicted or measured surface pressure to perturb the measured flat plate heating data, and accounts for "effective" boundary layer thinning due to the protrusion of the model into the boundary layer.

(5) The level and distribution of pressure on the floor of the RSI tile array gaps follow closely those of the external tile surface.

(6) Heat transfer to the gap wall is significantly higher at the intersection of a streamwise and transverse gap than for a single streamwise or transverse gap.

(7) Simulation of full-scale vehicle pressure gradient was good.

(8) For a thick turbulent boundary layer, there is no systematic effect of pressure gradient on tile array gap heat transfer.

VII. REFERENCES

1. Chapman, Dean R.: A Theoretical Analysis of Heat Transfer in Regions of Separated Flow. NACA TN 3792, October 1956.
2. Larson, Howard K.: Heat Transfer in Separated Flows. Journal of the Aerospace Sciences, Vol. 26, No. 11, pp 731-738, November 1959.
3. Charwat, A. F.; Roos, J. N.; Dewey, F. C., Jr.; and Hitz, J. A.: An Investigation of Separated Flows - Part I: The Pressure Field. Journal of the Aerospace Sciences, Vol. 28, No. 6, pp 457-470, June 1961.
4. Charwat, A. F.; Dewey, C. F., Jr.; Roos, J. N.; and Hitz, J. A.: An Investigation of Separated Flows - Part II: Flow in the Cavity and Heat Transfer. Journal of the Aerospace Sciences, Vol. 28, No. 7, pp 513-527, July 1961.
5. Nicoll, Kenneth M.: A Study of Laminar Hypersonic Cavity Flows. AIAA Journal, Vol. 2, No. 9, pp 1535-1541, September 1964.
6. Emery, A. F.; Sadunas, J. A.; and Loll, M.: Heat Transfer and Pressure Distribution in Open Cavity Flow. Journal of Heat Transfer, pp 103-108, February 1967.
7. Hahn, Mansop: Experimental Investigation of Separated Flow Over a Cavity at Hypersonic Speed. AIAA Journal, Vol. 7, No. 6, pp 1092-1098, June 1969.
8. Nestler, D. E.: Laminar Heat Transfer to Cavities in Hypersonic Low Density Flow. Proceedings of the 3rd International Heat Transfer Conference, Vol. 2, AIChE, New York, 1966.
9. Wieting, Allan R.: Experimental Investigation of Heat-Transfer Distributions in Deep Cavities in Hypersonic Separated Flow. NASA TN D-5908, September 1970.
10. Hodgson, J. W.: Heat Transfer in Separated Laminar Hypersonic Flow. AIAA Journal, Vol. 8, No. 12, pp 2291-2293, December 1970.
11. Rhudy, J. P.; and Magnan, J. D., Jr.: Investigation of Heat-Transfer Distribution in Several Cavity and Step Configurations at Mach 10. AEDC-TDR-64-220, October 1964.
12. Haugen, R. L.; and Dhanak, A. M.: Momentum Transfer in Turbulent Separated Flow Past a Rectangular Cavity. Journal of Applied Mechanics, pp 641-646, September 1966.

13. Haugen, R. L.; and Dhanak, A. M.: Heat Transfer in Turbulent Boundary-Layer Separation Over a Surface Cavity. *Journal of Heat Transfer*, pp 335-340, November 1967.
14. Nestler, D. E.; Saydah, A. R.; and Auxer, W. L.: Heat Transfer to Steps and Cavities in Hypersonic Turbulent Flow. *AIAA Journal*, Vol. 7, No. 7, pp 1368-1370, July 1969.
15. Winkler, Eva M.; Humphrey, Richard L.; Madden, Michael T.; and Koenig, Joseph A.: Substructure Heating on Cracked Ablative Heat Shields. *AIAA Journal*, Vol. 8, No. 10, pp 1895-1896, October 1970.
16. Burggraf, Odus R.: A Model of Steady Separated Flow in Rectangular Cavities at High Reynolds Number. *Proceedings of the 1965 Heat Transfer and Fluid Mechanics Inst.*, A. F. Charwat, ed., Stanford Univ. Press, 1965, pp 190-229.
17. Nestler, D. E.: Hypersonic Laminar Cavity Heat Transfer. Presented to the 4th International Heat Transfer Conference, Versailles, September 1970.
18. Nestler, D. E.: An Engineering Analysis of Reattaching Shear Layer Heat Transfer. *AIAA Paper No. 72-717*, June 1972.
19. Brewer, R. A.; Saydah, A. R.; Nestler, D. E.; and Foster, Thomas F.: Thermal Performance Evaluation of RSI Panel Gaps for Space Shuttle Orbiter. *Journal of Spacecraft and Rockets*, Vol. 10, No. 1, pp 23-28, January 1973.
20. Johnson, Charles B.: Heat Transfer Data to Cavities Between Simulated RSI Tiles at Mach 8. *NASA CR-128,770*, Space Shuttle DMS-DR-2043, June 1973.
21. Throckmorton, David A.: Heat Transfer to Surface and Gaps of RSI Tile Arrays in Turbulent Flow at Mach 10.3. *NASA TM X-71945*, April 1974.
22. Foster, Thomas F.; Lockman, William K.; and Grifall, William J.: Thermal Protection System Gap Heating Rates of the Rockwell International Flat Plate Heat Transfer Model. *NASA CR-134,077*, Space Shuttle DMS-DR-2035, November 1973.
23. Christensen, H. E.; Kipp, H. W.; and Steele, J. R.: Data Correlation and Analysis of Arc Tunnel and Wind Tunnel Tests of RSI Joints and Gaps. *MDC E10003 - JSC 09003*, Final Report, Contract NAS9-13439, McDonnell Douglas Corporation, January 1974.

24. Ames Research Staff: Equations, Tables, and Charts for Compressible Flow. NACA Report 1135, 1953.
25. Erickson, Wayne D.; and Creekmore, Helen S.: A Study of Equilibrium Real-Gas Effects in Hypersonic Air Nozzles, Including Charts of Thermodynamic Properties for Equilibrium Air. NASA TN D-231, April 1960.
26. Bushnell, Dennis M.; and Johnson, Charles B.: Comparison of Prediction Methods and Studies of Relaxation in Hypersonic Turbulent Nozzle-Wall Boundary Layers. NASA TN D-5433, 1969.
27. Nicoll, Kenneth M.: Use of Transient "Thin-Wall" Technique in Measuring Heat Transfer Rates in Hypersonic Separated Flows. AIAA Journal, Vol. 1, No. 4, April 1963.
28. Eckert, E. R. G.; and Drake, R. M., Jr.: Heat and Mass Transfer. McGraw-Hill Book Company, New York, 1959.
29. Dunavant, James C.; and Throckmorton, David A.: Aerodynamic Heat Transfer to RSI Tile Surfaces and Gap Intersections. Journal of Spacecraft and Rockets, Vol. 11, No. 6, June 1974.
30. Carslaw, H. S., and Jaeger, J. C.: Conduction of Heat in Solids. Second edition, Oxford University Press, Inc., 1959.

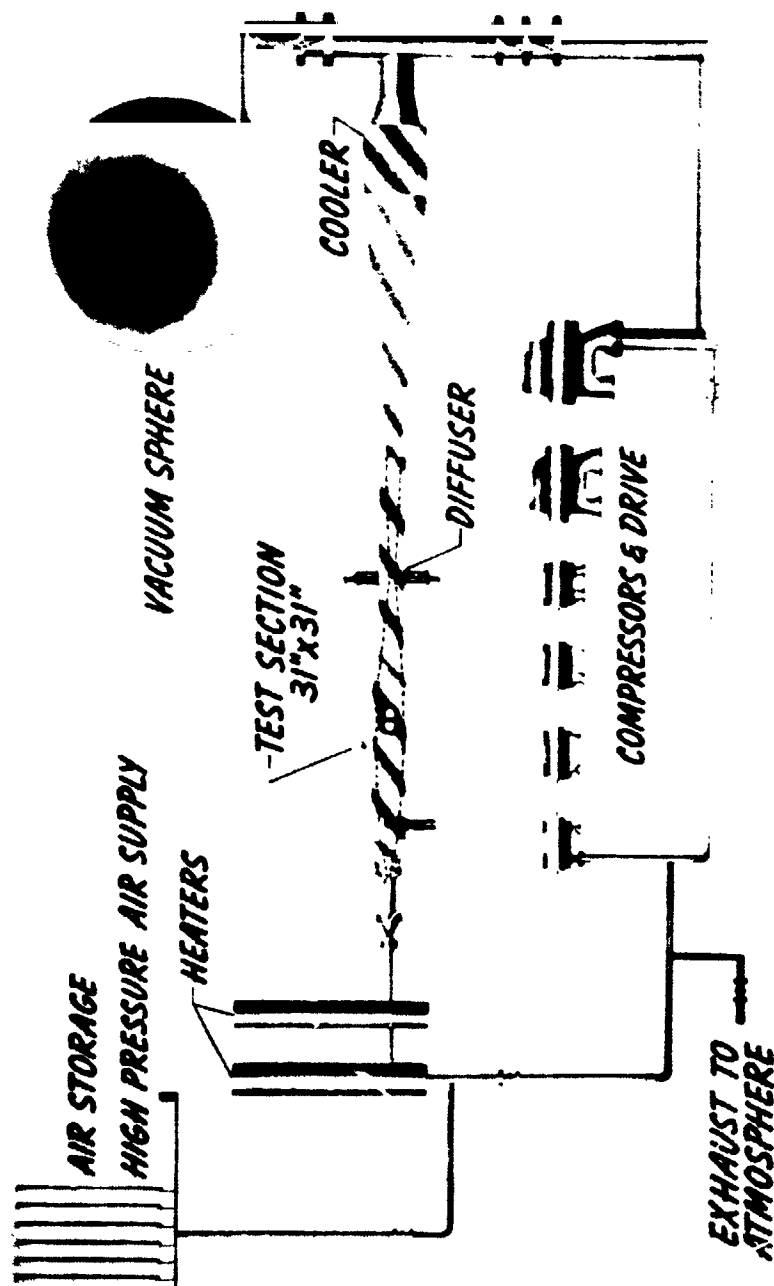


Figure 1.- Schematic diagram of + facility.

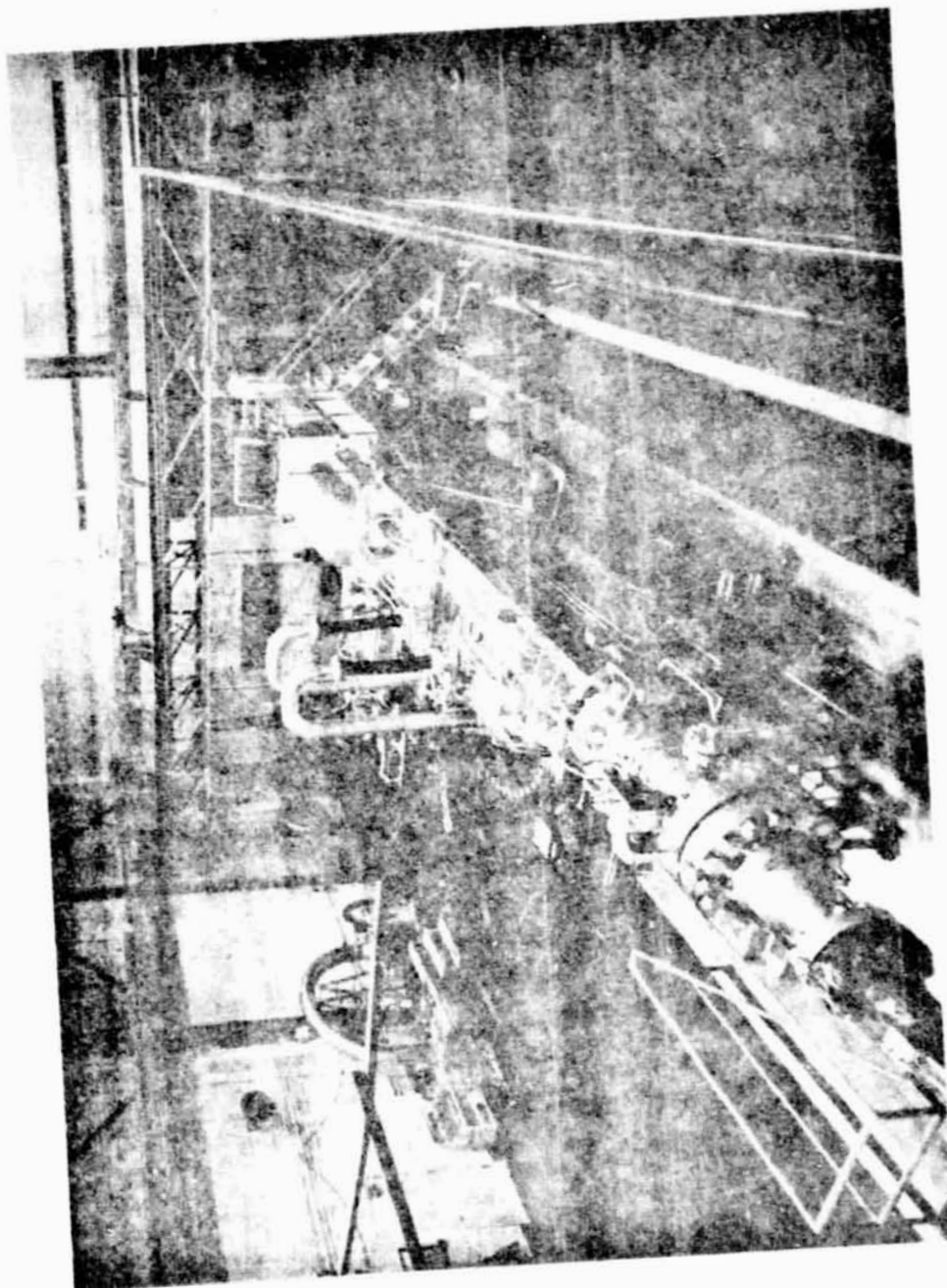
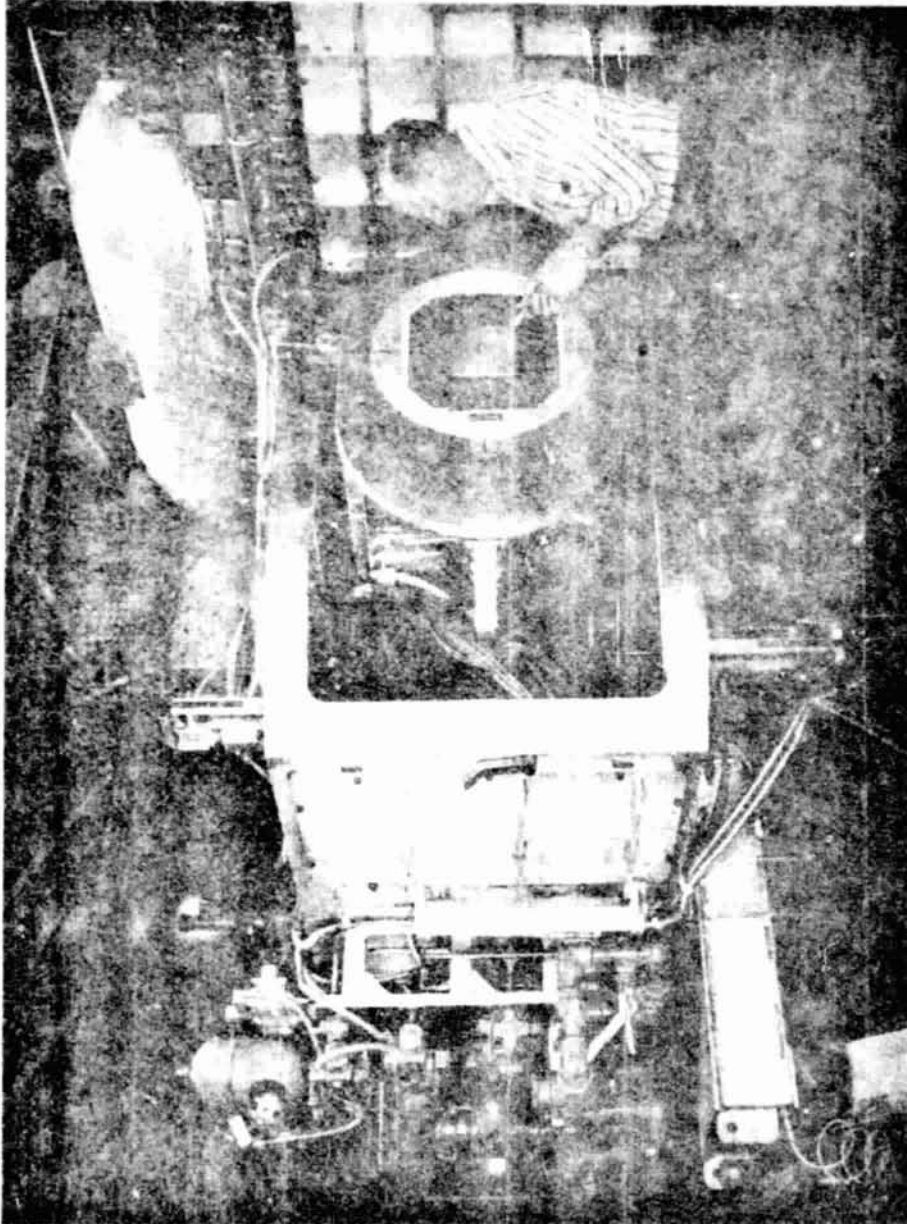


Figure 2.- Langley Continuous Flow Hypersonic Tunnel.

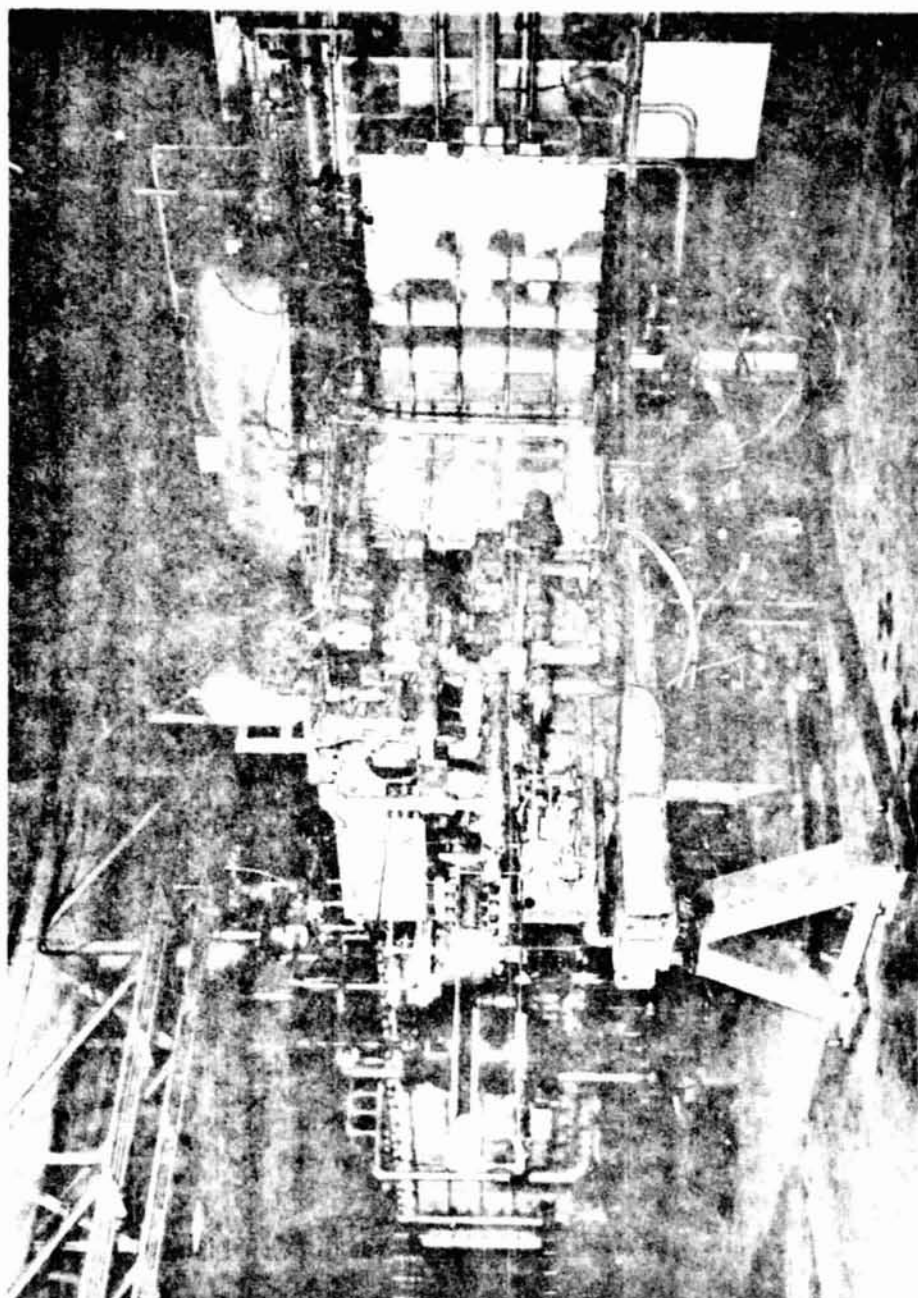
REPRODUCIBILITY OF THE
ORIGINAL PAGE IS POOR



(a) Model access position.

Figure 3.- Model injection mechanism.

REPRODUCIBILITY OF THE
ORIGINAL PAGE IS POOR.



(b) Rotated to test position.

Figure 3.- Concluded.

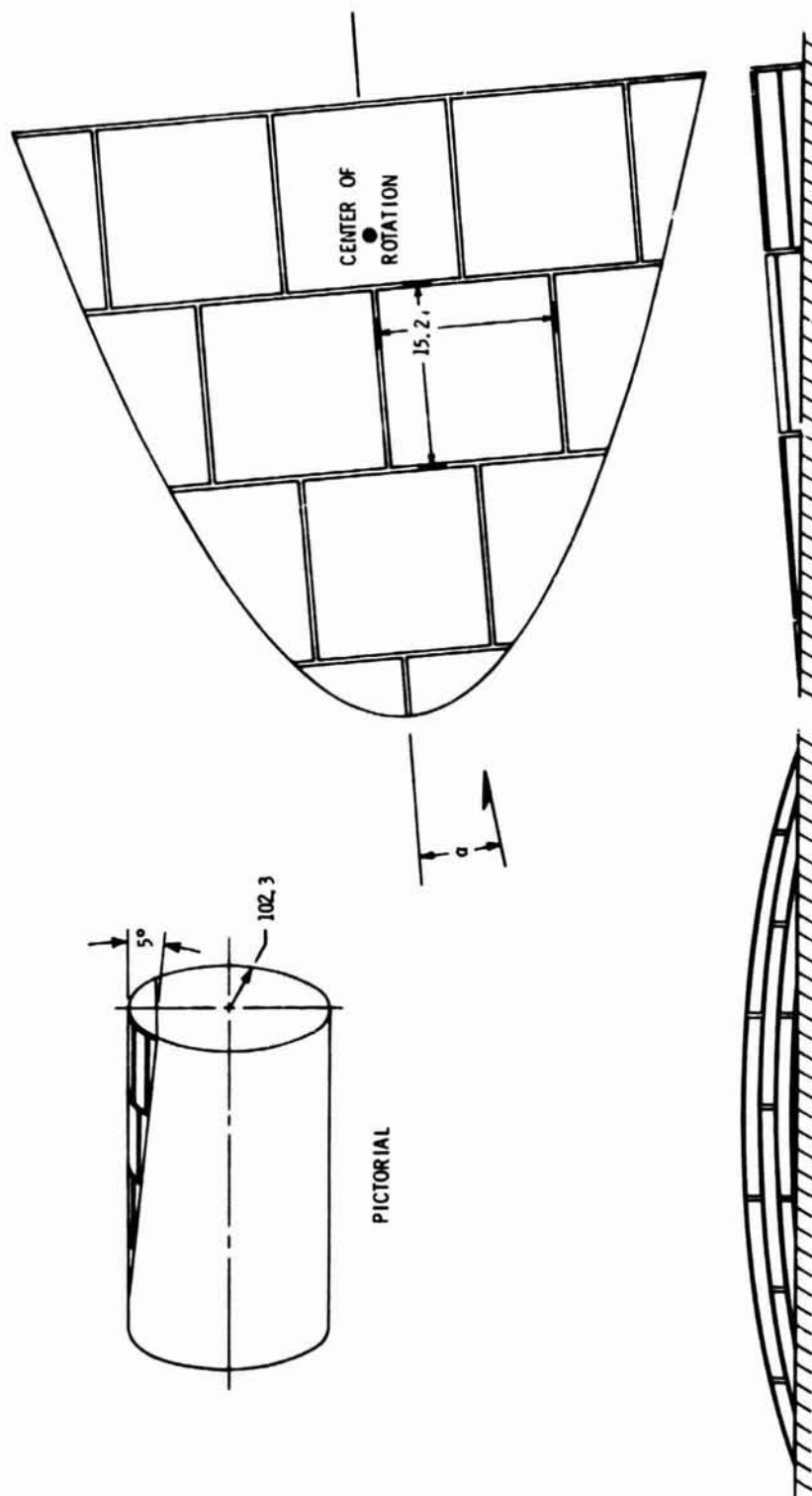


Figure 4.- RSI pressure gradient model schematic.

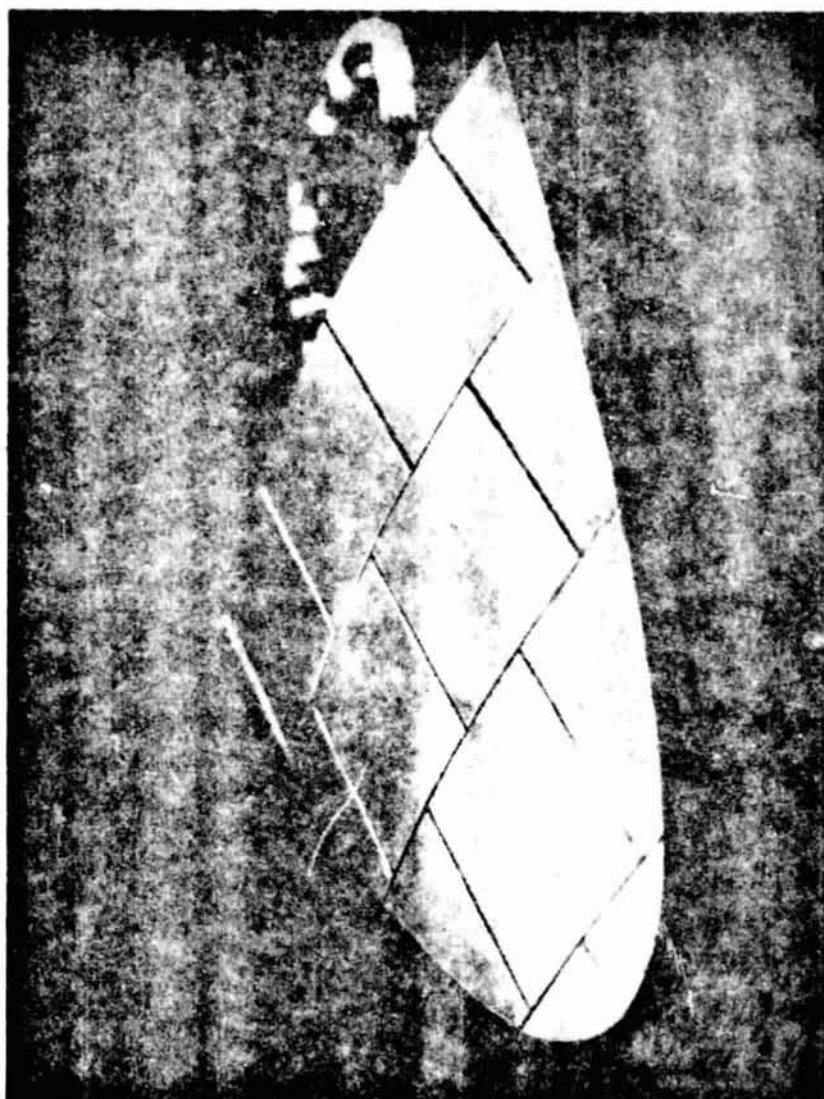
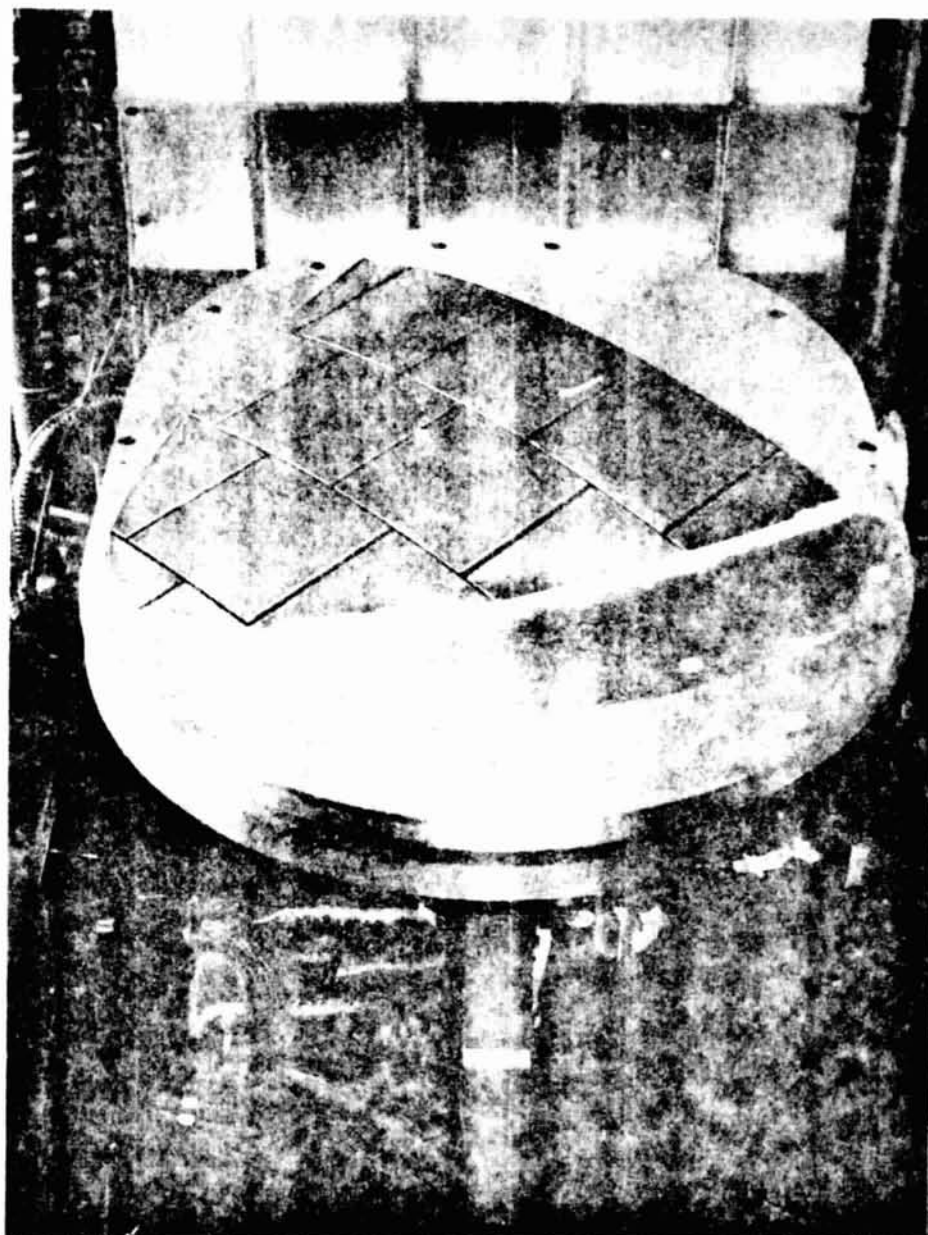


Figure 5.- RSI pressure gradient model.

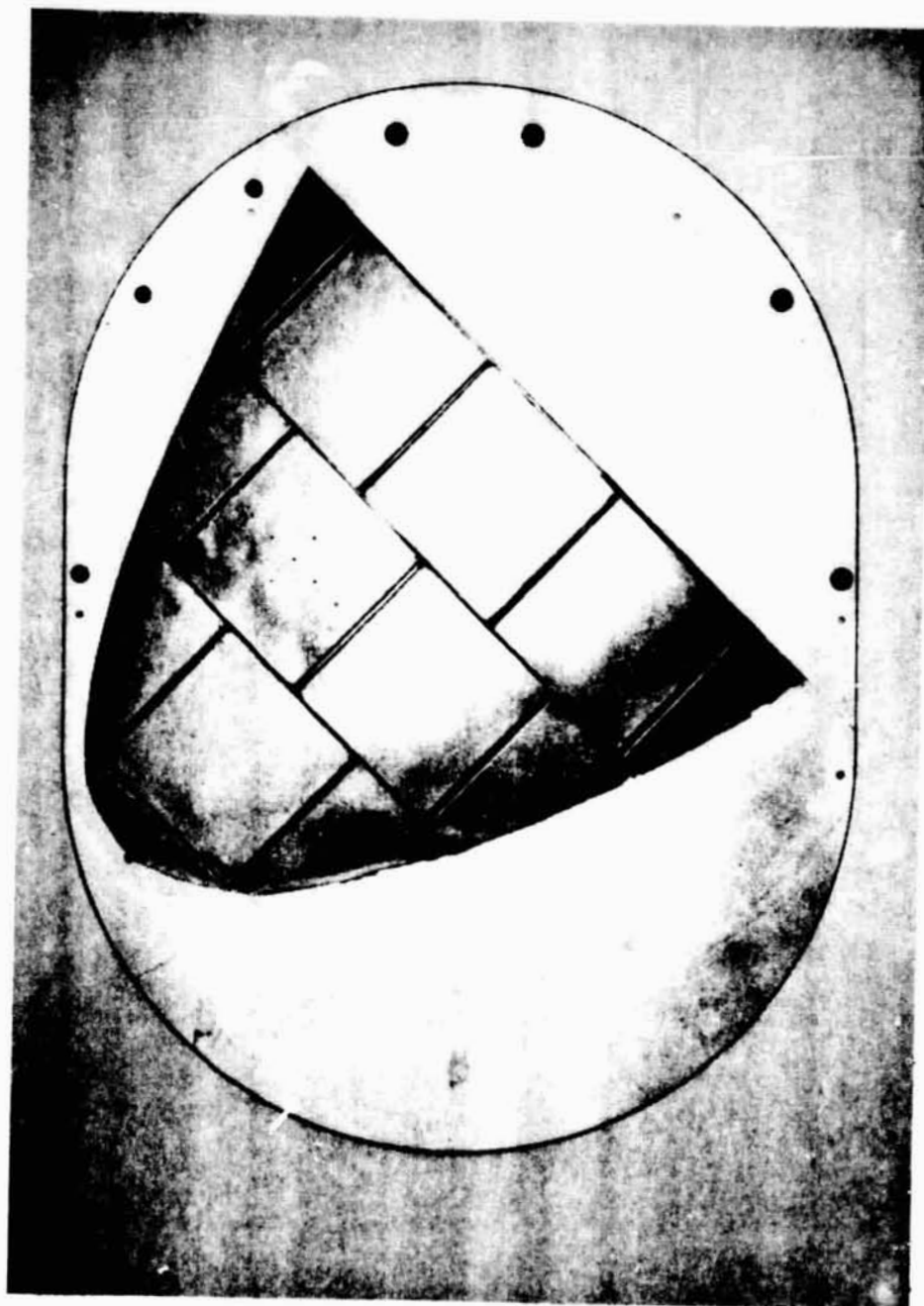
REPRODUCIBILITY OF THE
ORIGINAL PAGE IS POOR



(a) Model access position.

Figure 6.- RSI pressure gradient model mounted on injection strut.

REPRODUCIBILITY OF THE
ORIGINAL PAGE IS POOR



(b) Model in test position.

Figure 6.- Concluded.

REPRODUCIBILITY OF THE
ORIGINAL PAGE IS POOR.

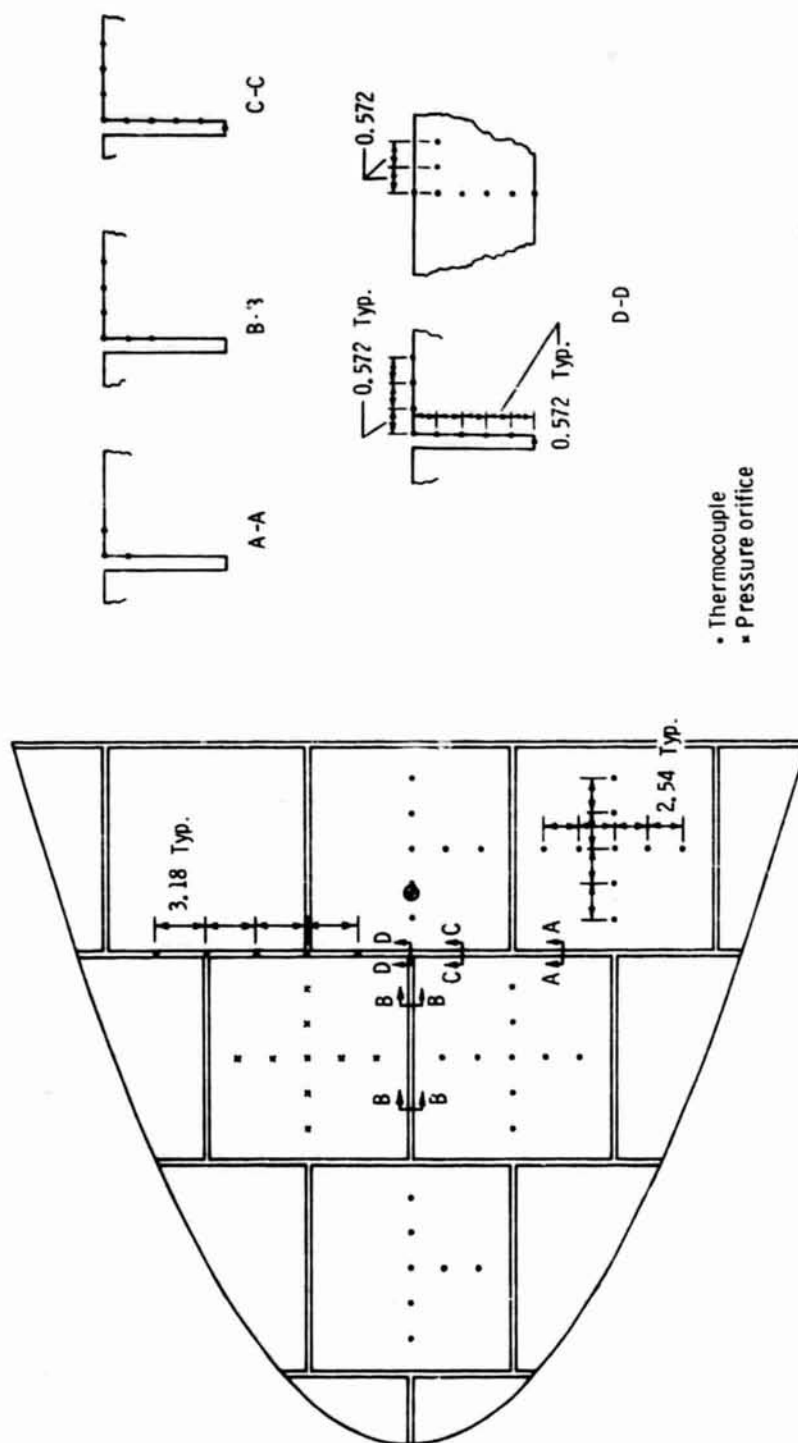


Figure 7.- RSI pressure gradient model instrumentation locations.

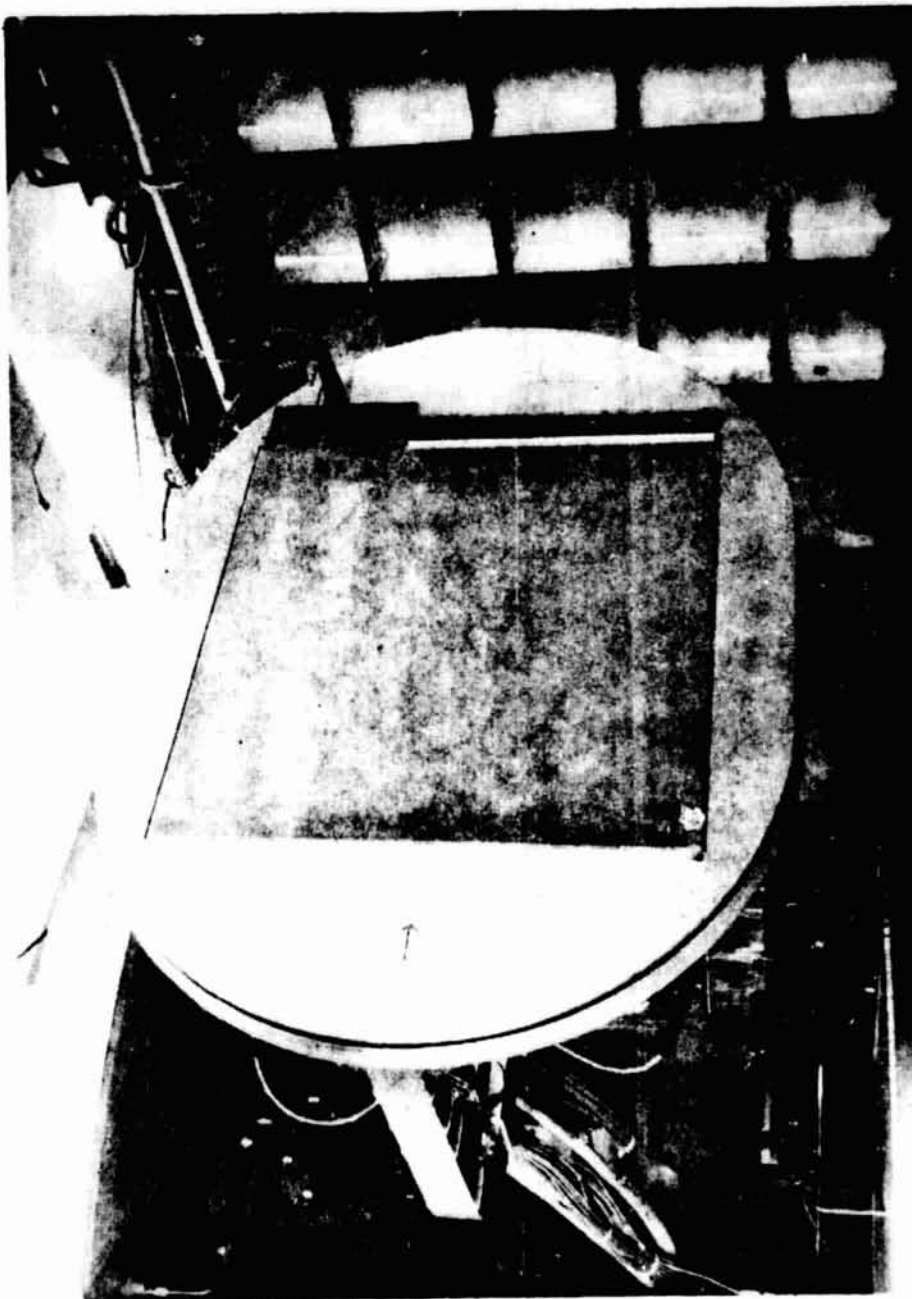


Figure 8.- Flat plate model mounted on injection strut.

REPRODUCIBILITY OF THE
ORIGINAL PAGE IS POOR

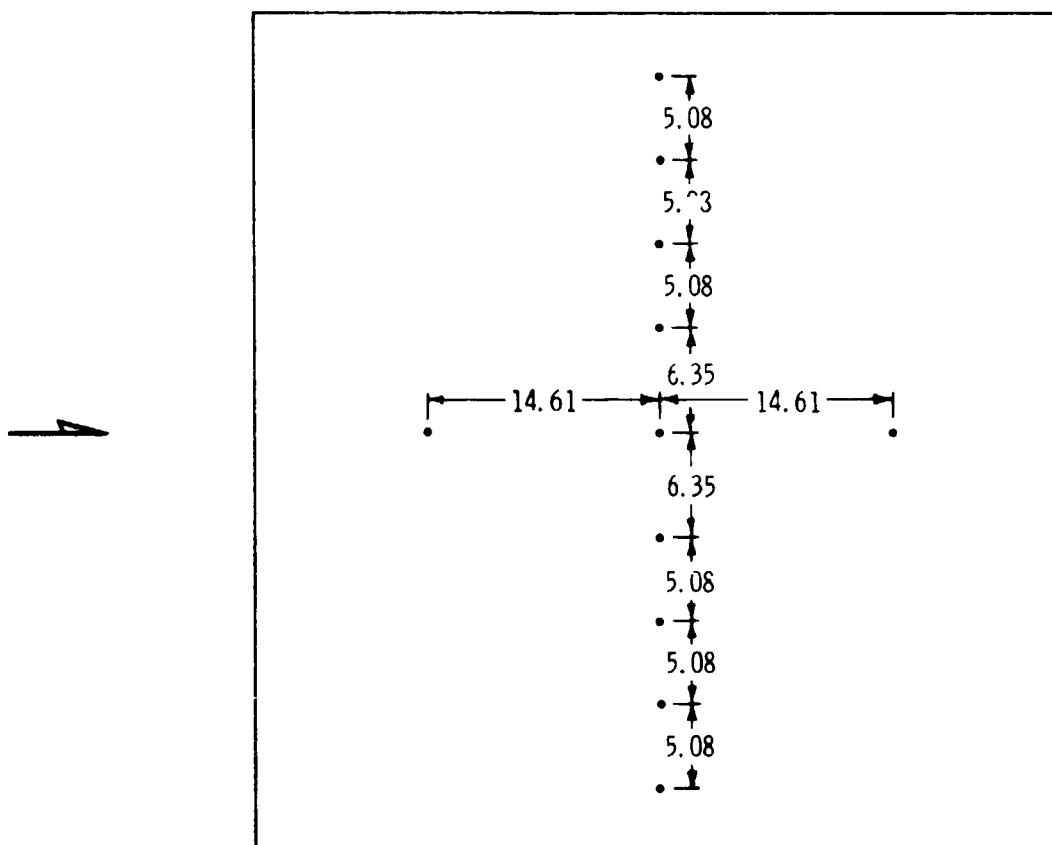


Figure 9.- Flat plate model instrumentation locations.

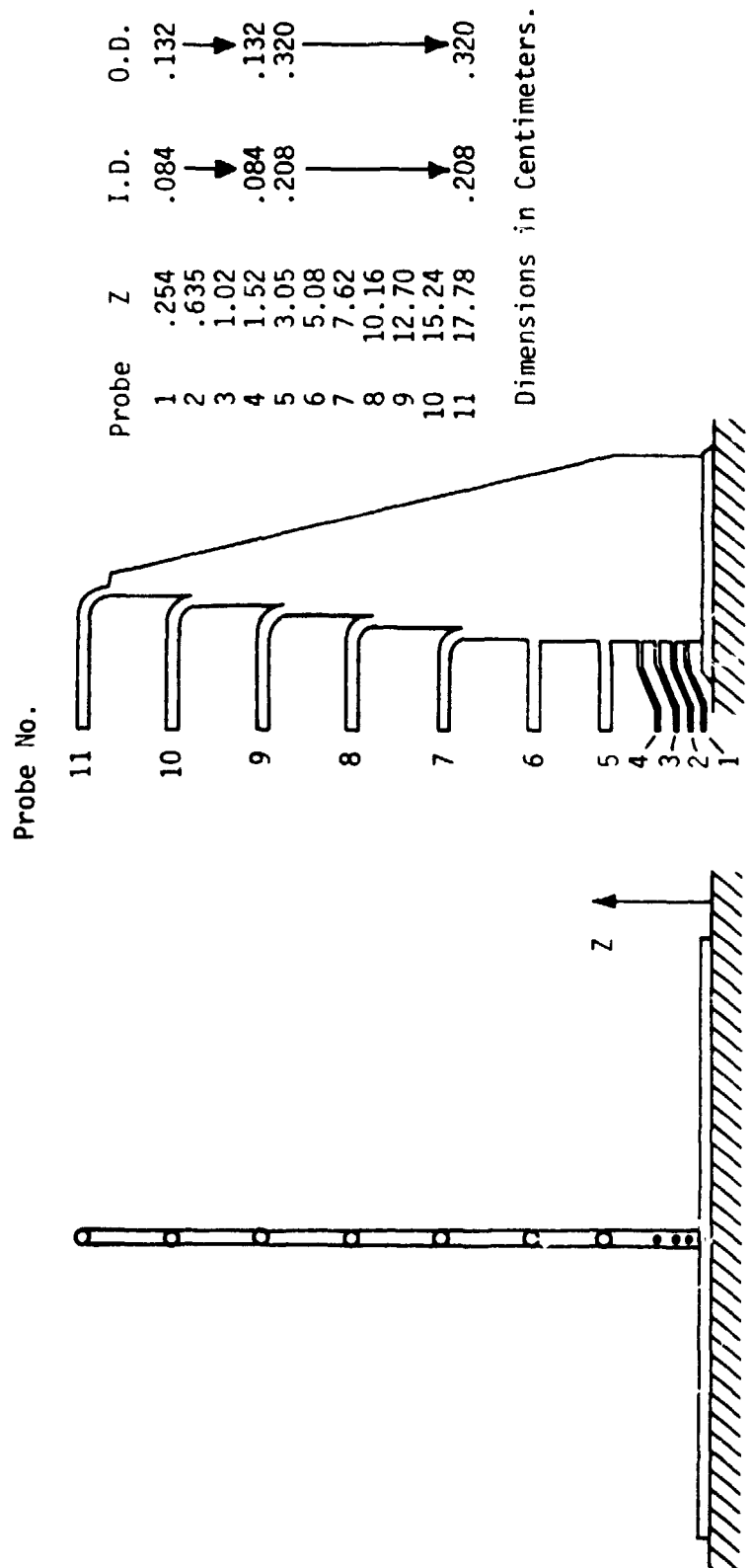


Figure 10.- Boundary layer pitot probe schematic.

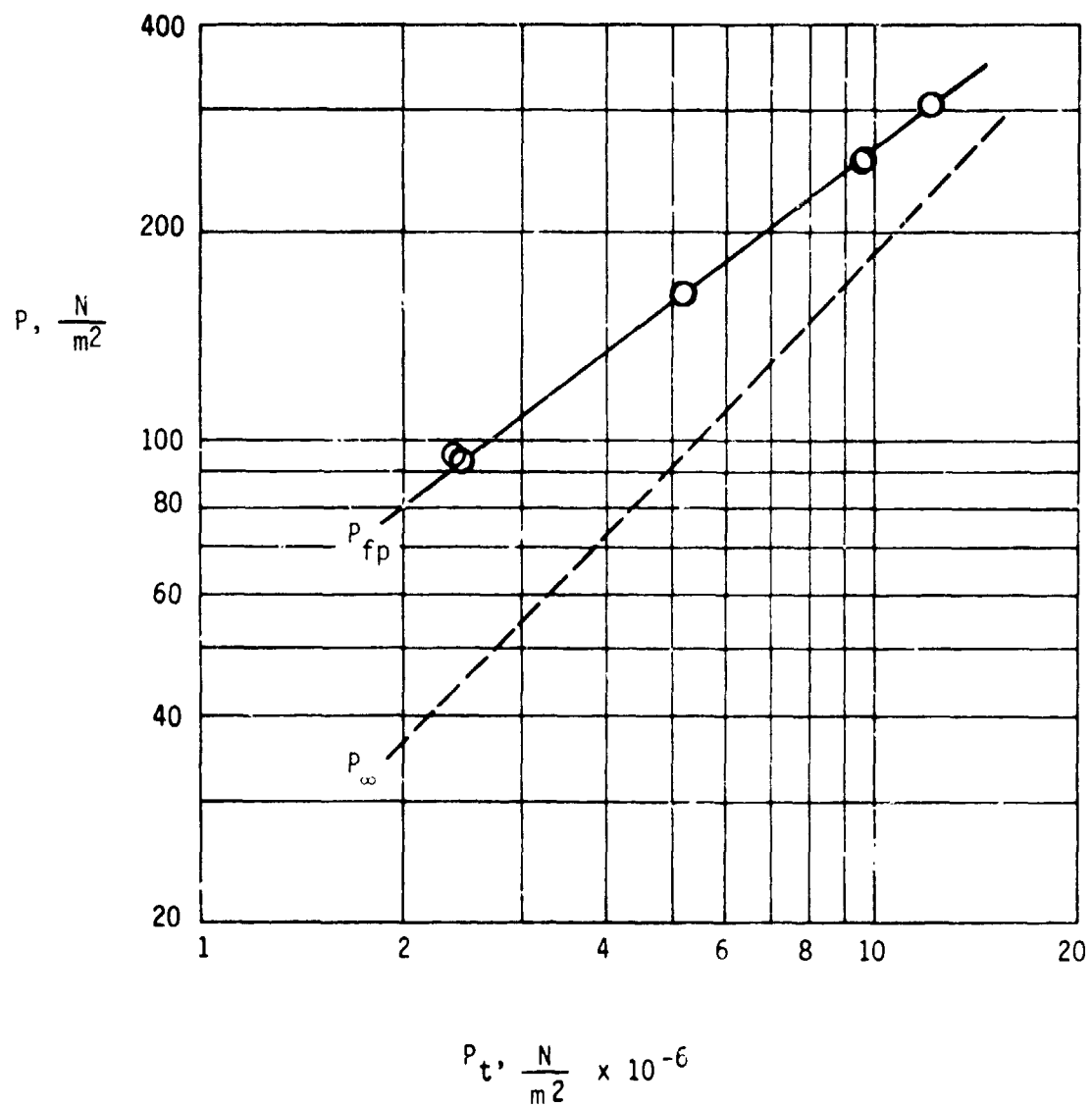


Figure 11.- Comparison of centerline wall and freestream static pressures.

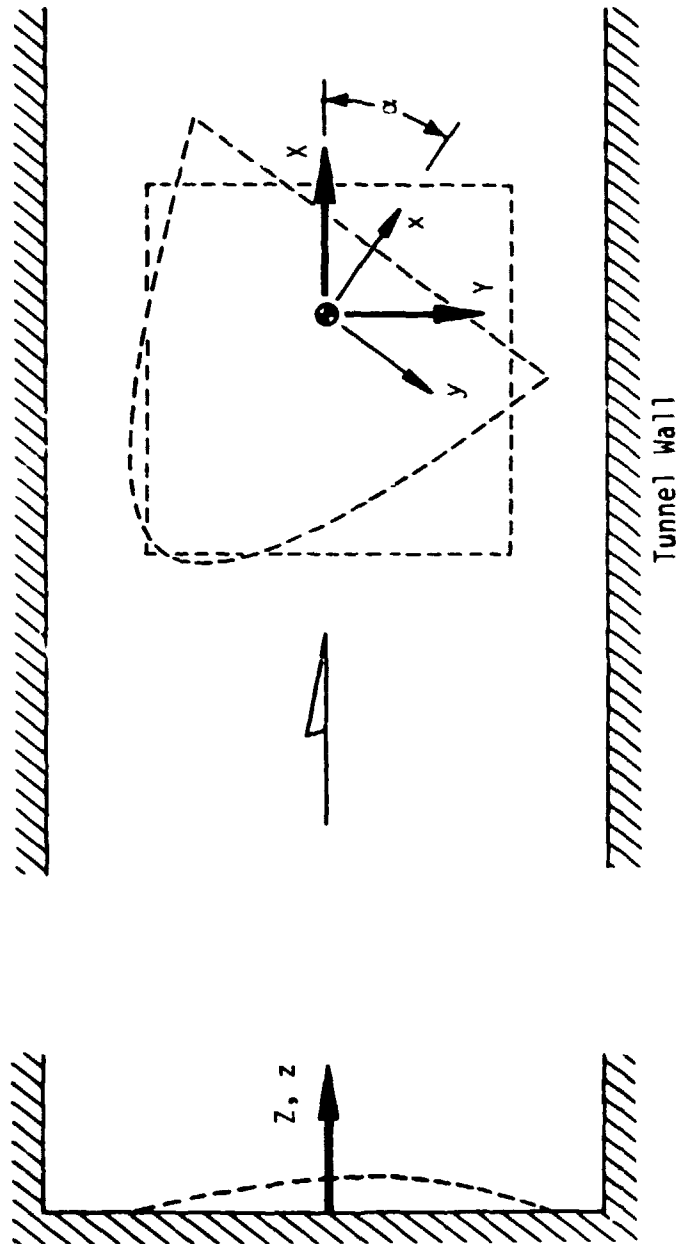


Figure 12.- Definition of coordinate systems.

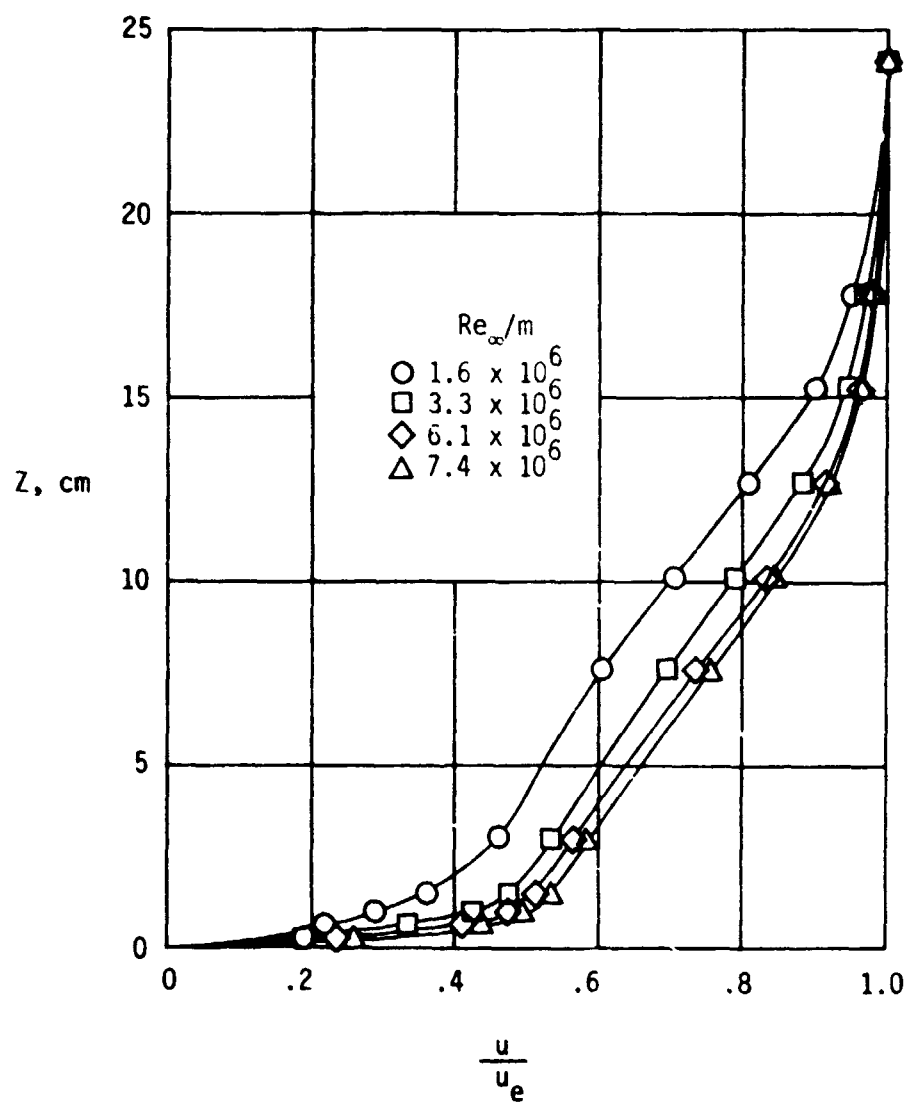


Figure 13.- Boundary layer velocity profiles at sidewall centerline. $Y = 0$.

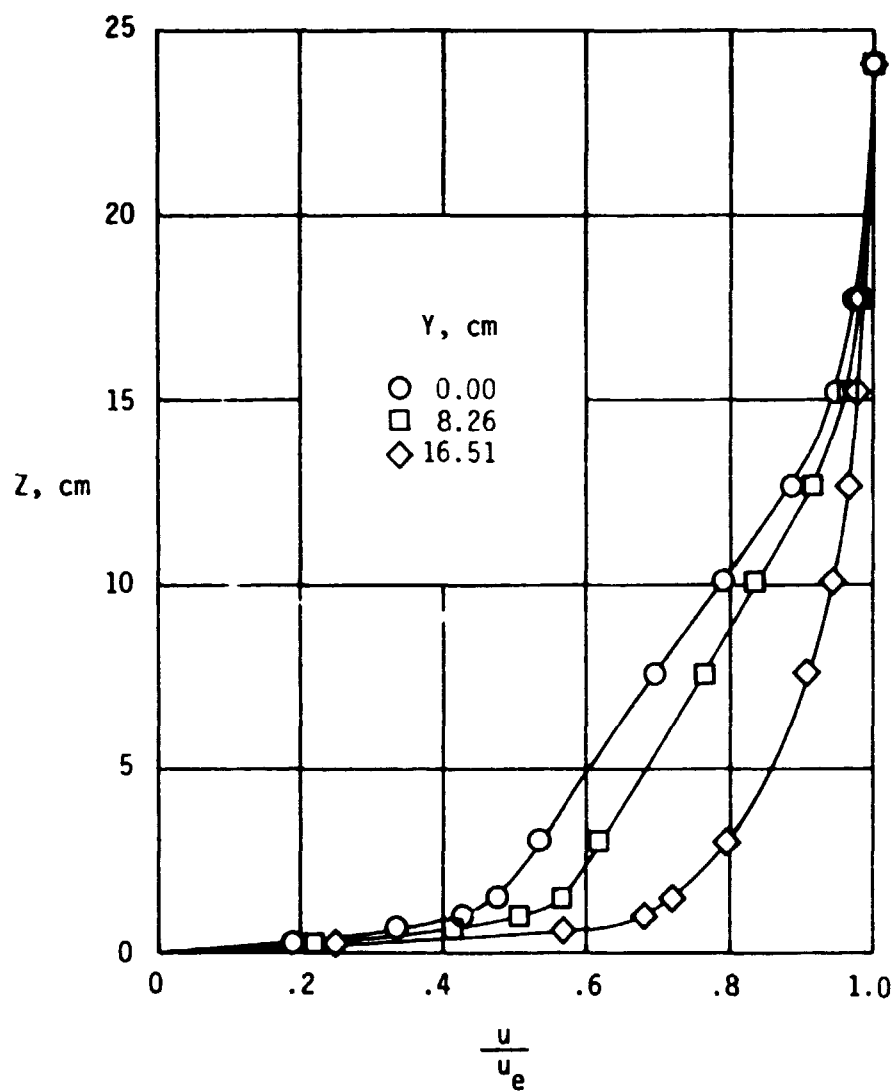


Figure 14.- Transverse variation of boundary layer velocity profile. $Re_{\infty}/m = 3.3 \times 10^6$.

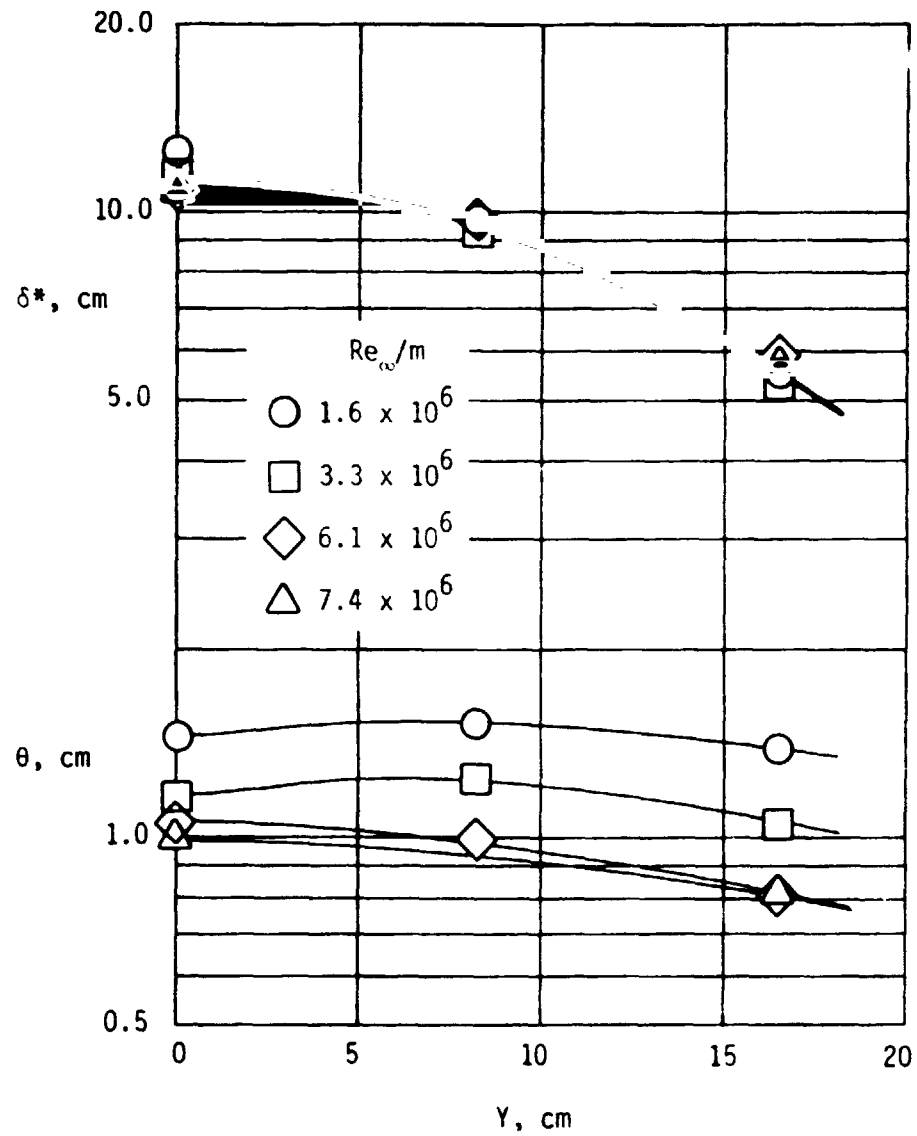


Figure 15.- Variation of displacement and momentum thicknesses with transverse wall position.

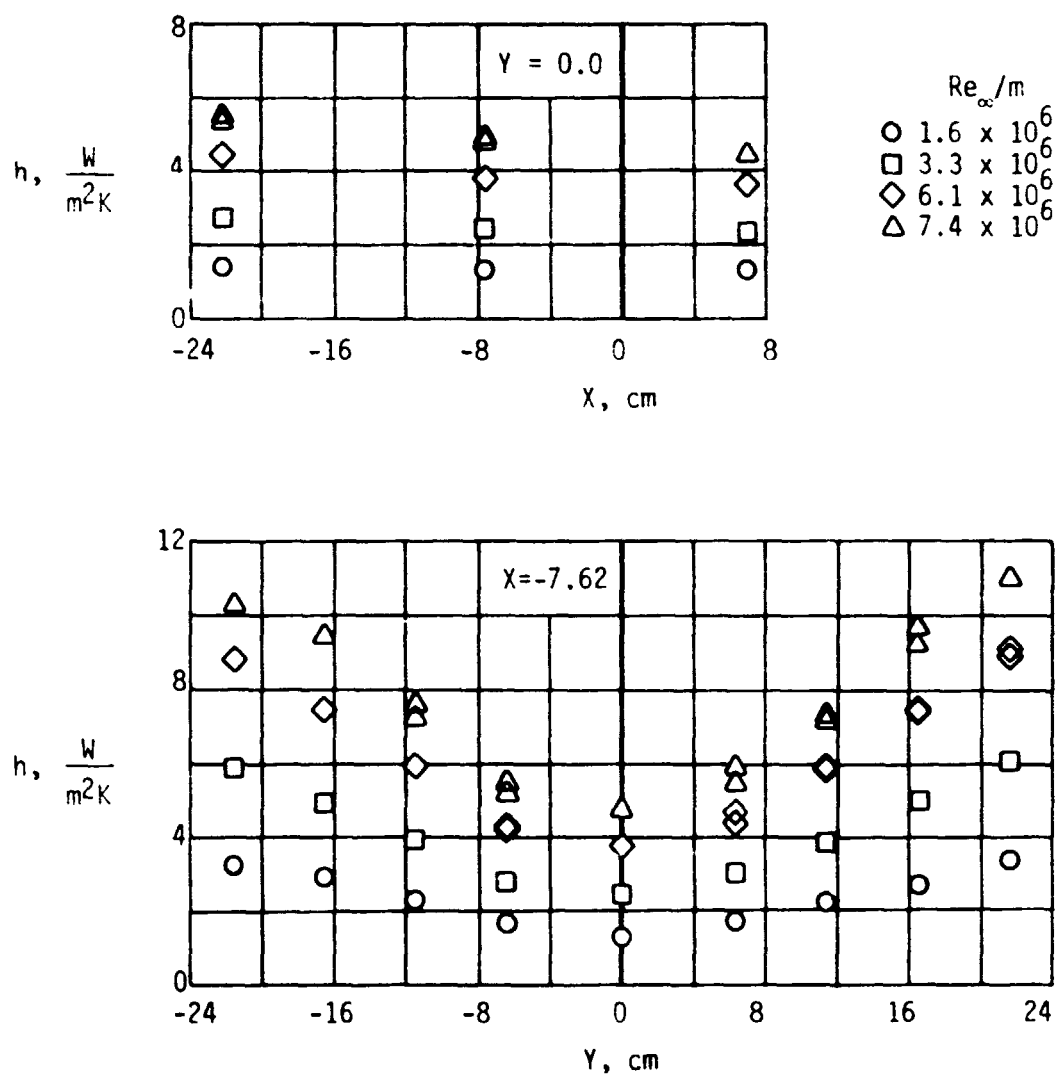


Figure 16.- Heat transfer coefficient distribution on the flat plate.

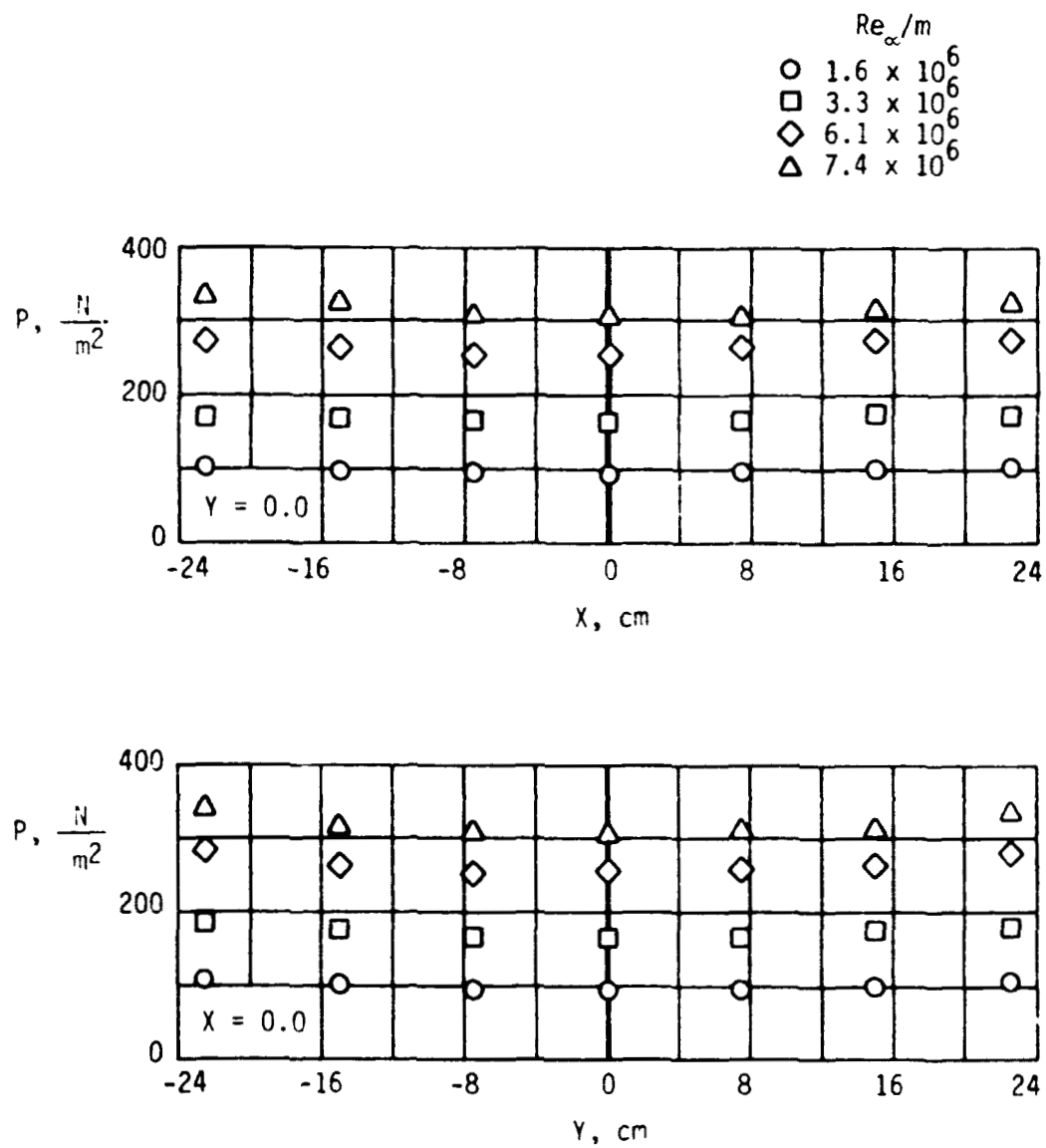


Figure 17.- Static pressure distribution on the flat plate.

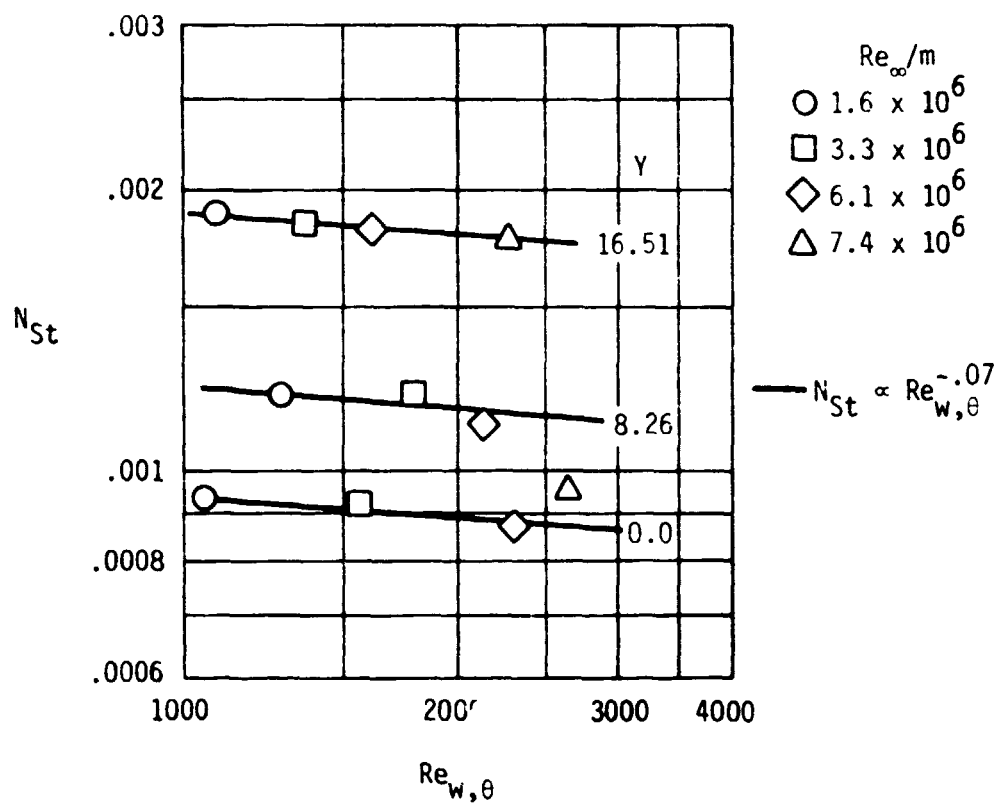


Figure 18.- Variation of flat plate Stanton number with momentum thickness Reynolds number.

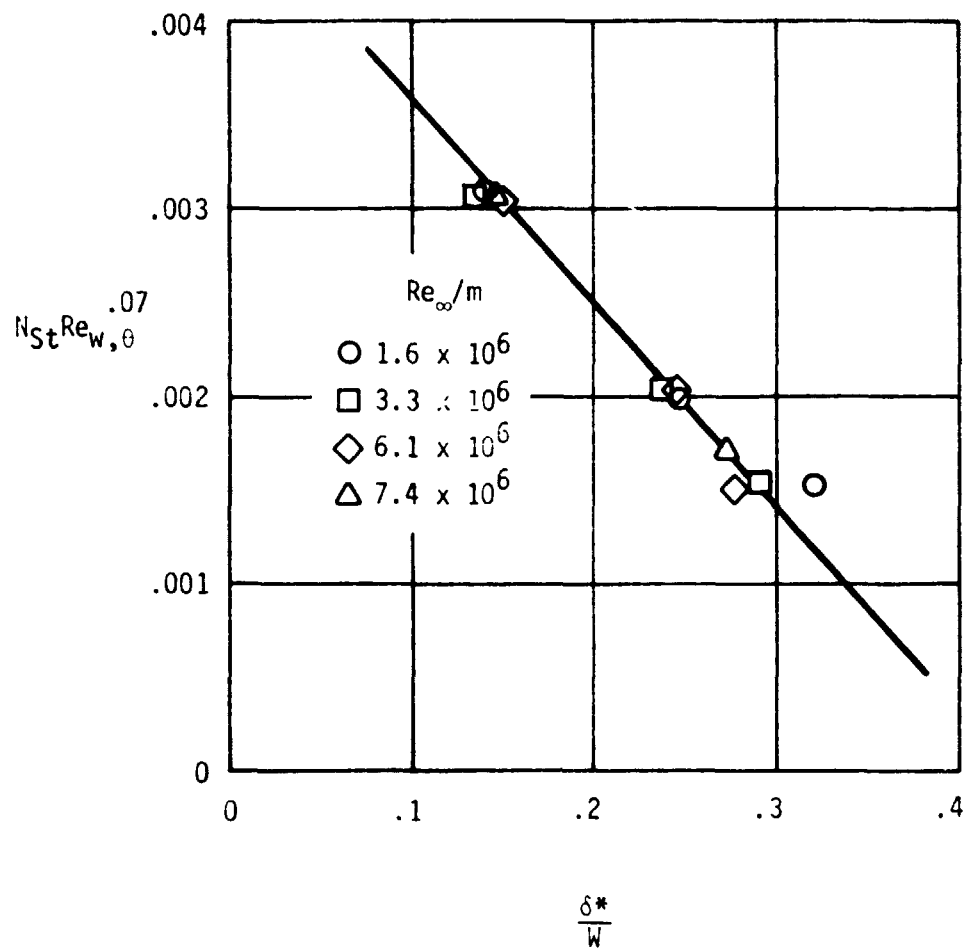


Figure 19.- Correlation of flat plate heat transfer with displacement thickness.

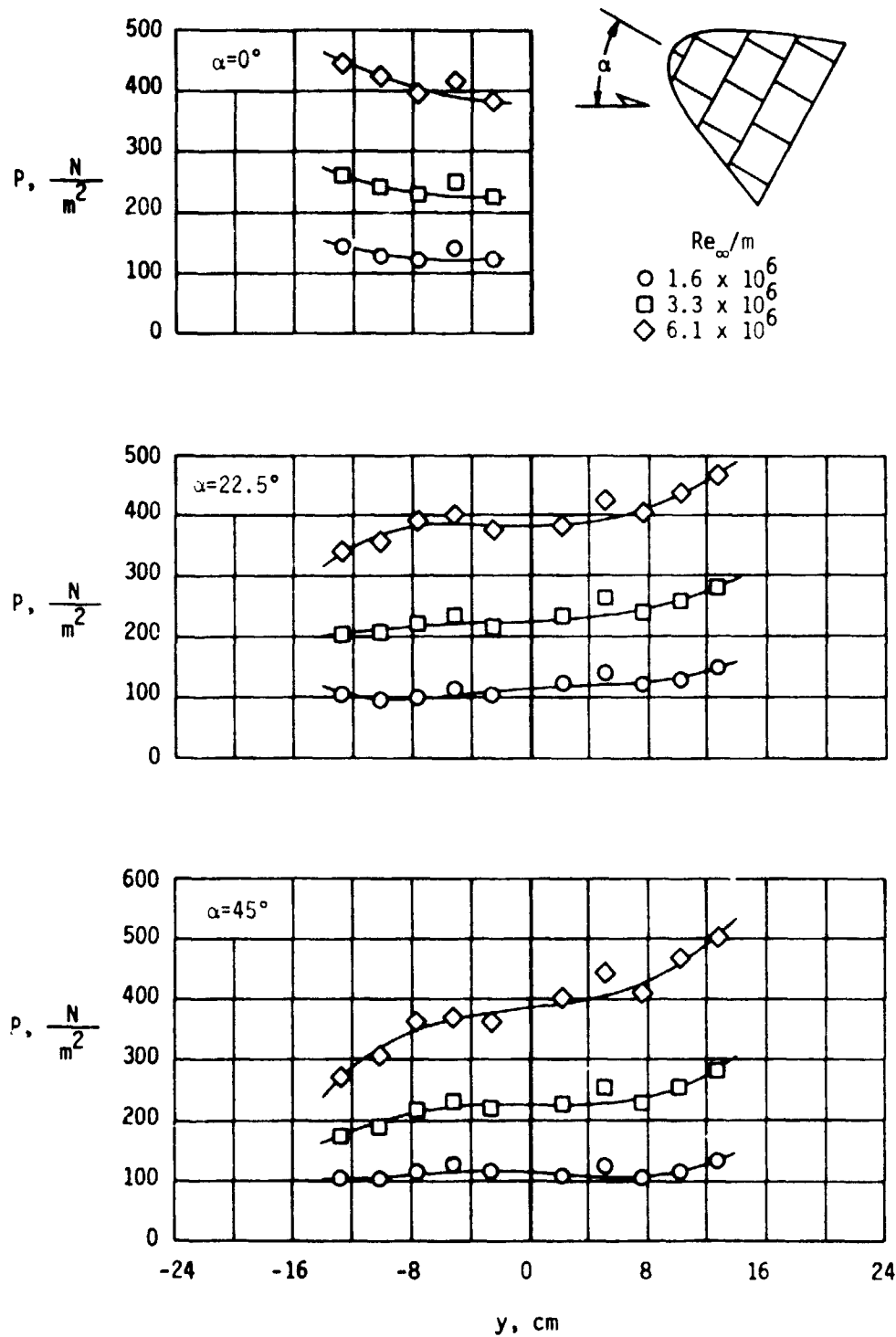
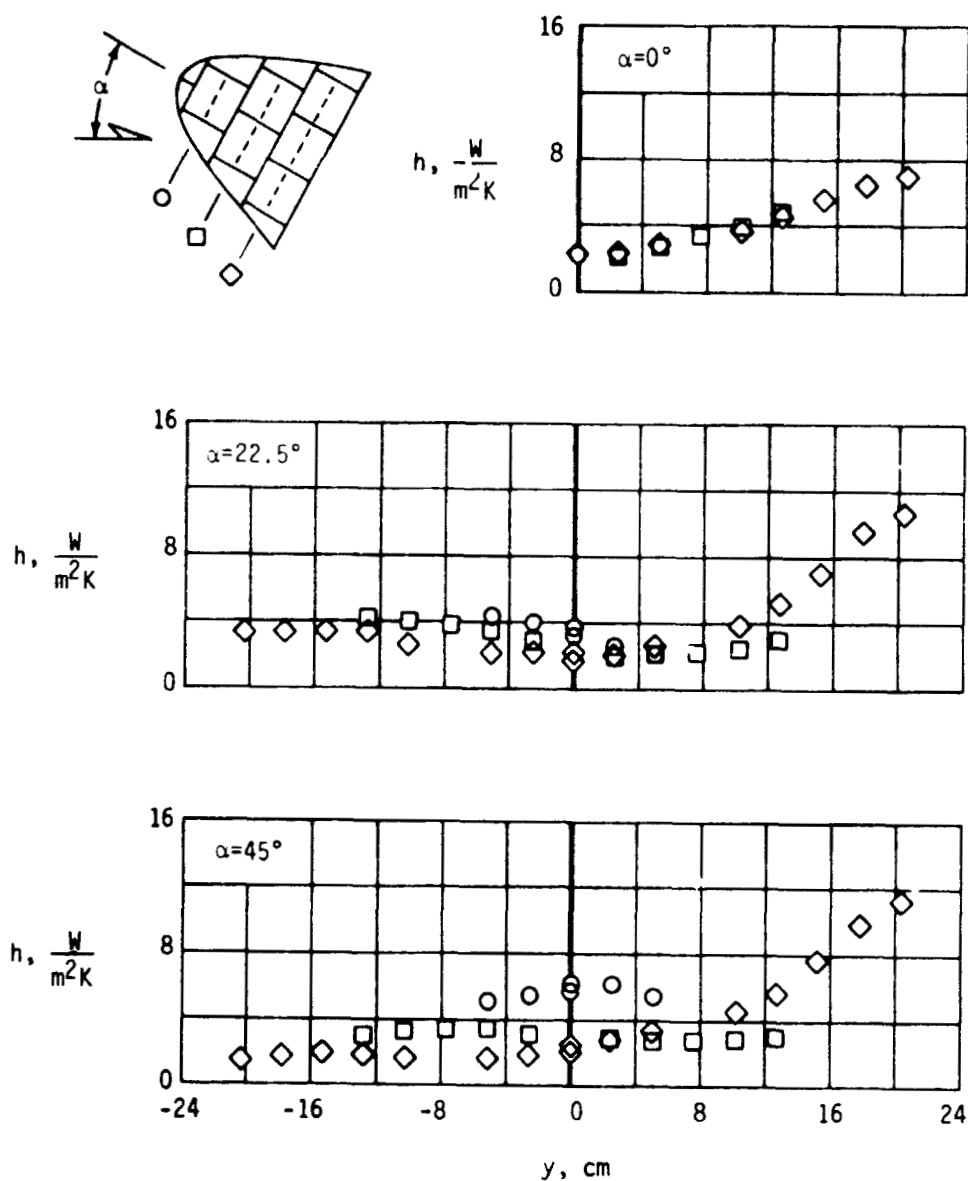
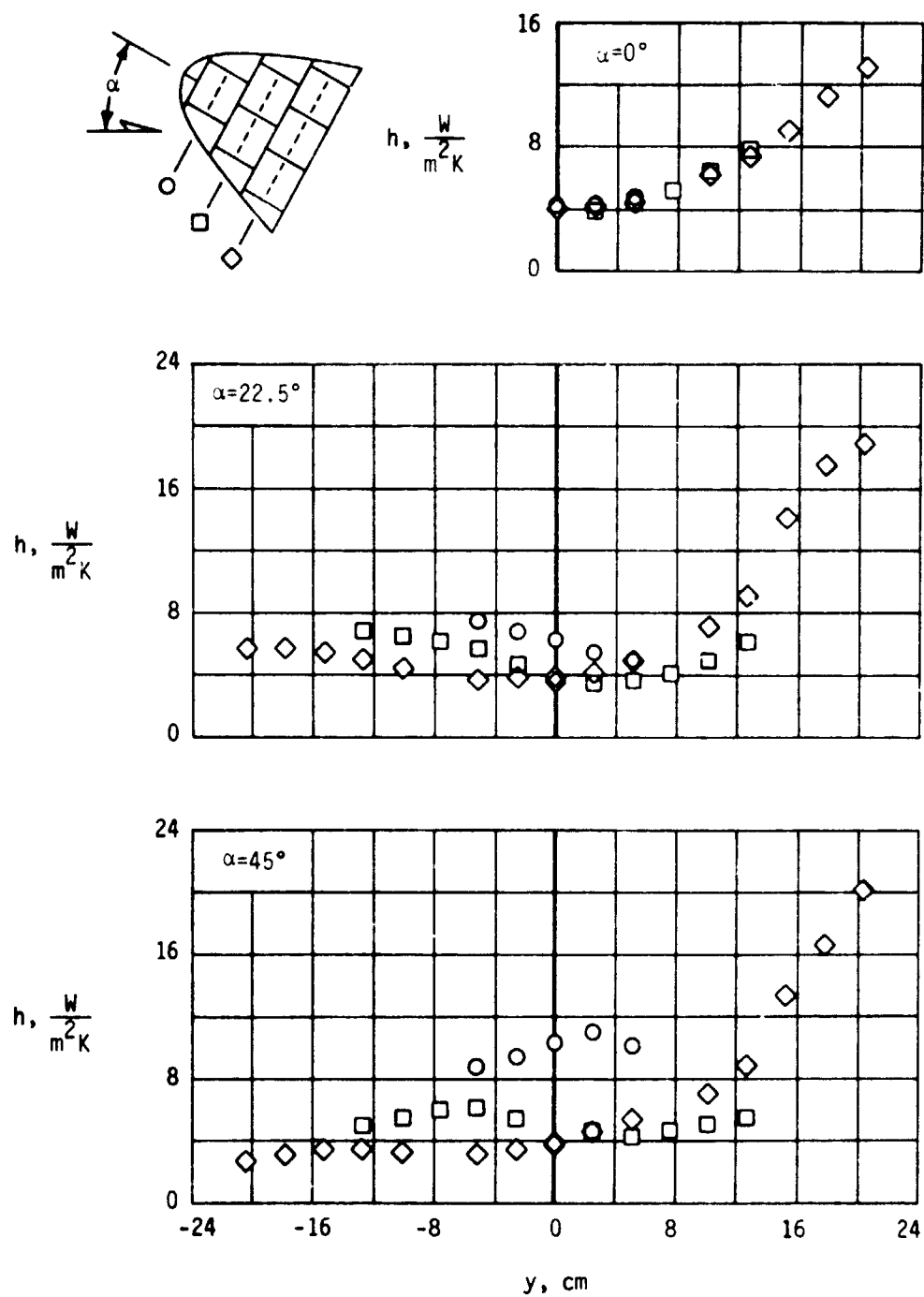


Figure 20.- Static pressure distributions on the smoothed RSI tile array model.



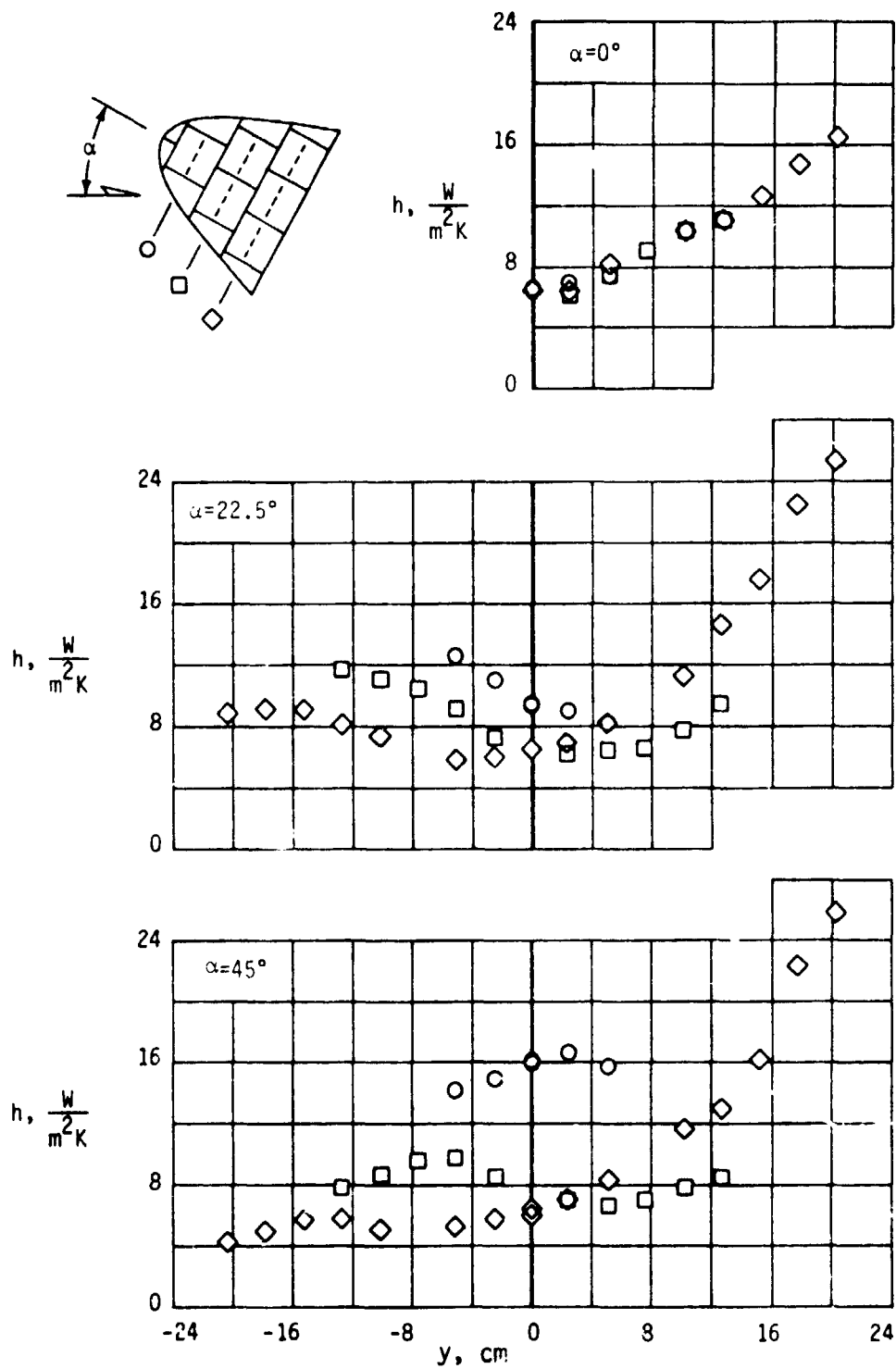
(a) $Re_\infty/m = 1.6 \times 10^6$.

Figure 21.- Surface heat transfer distributions on the smoothed RSI tile array model.



(b) $\text{Re}_\infty/m = 3.3 \times 10^6$.

Figure 21.- Continued.



(c) $Re_\infty/m = 6.1 \times 10^6$.

Figure 21.- Concluded.

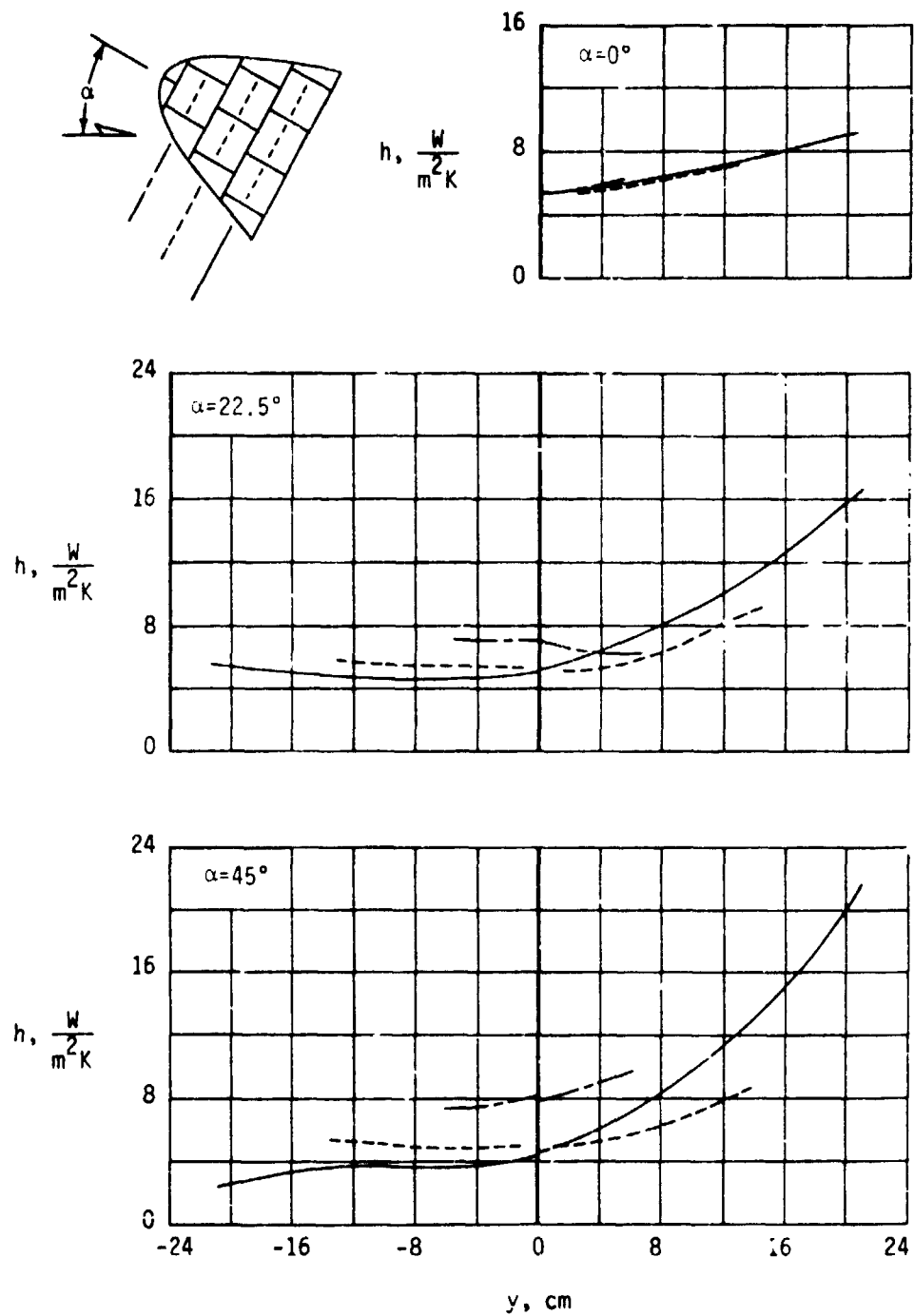


Figure 22.- Predicted heat transfer to the smoothed RSI tile array model assuming modified Newtonian pressure.
 $Re_\infty/m = 3.3 \times 10^6$.

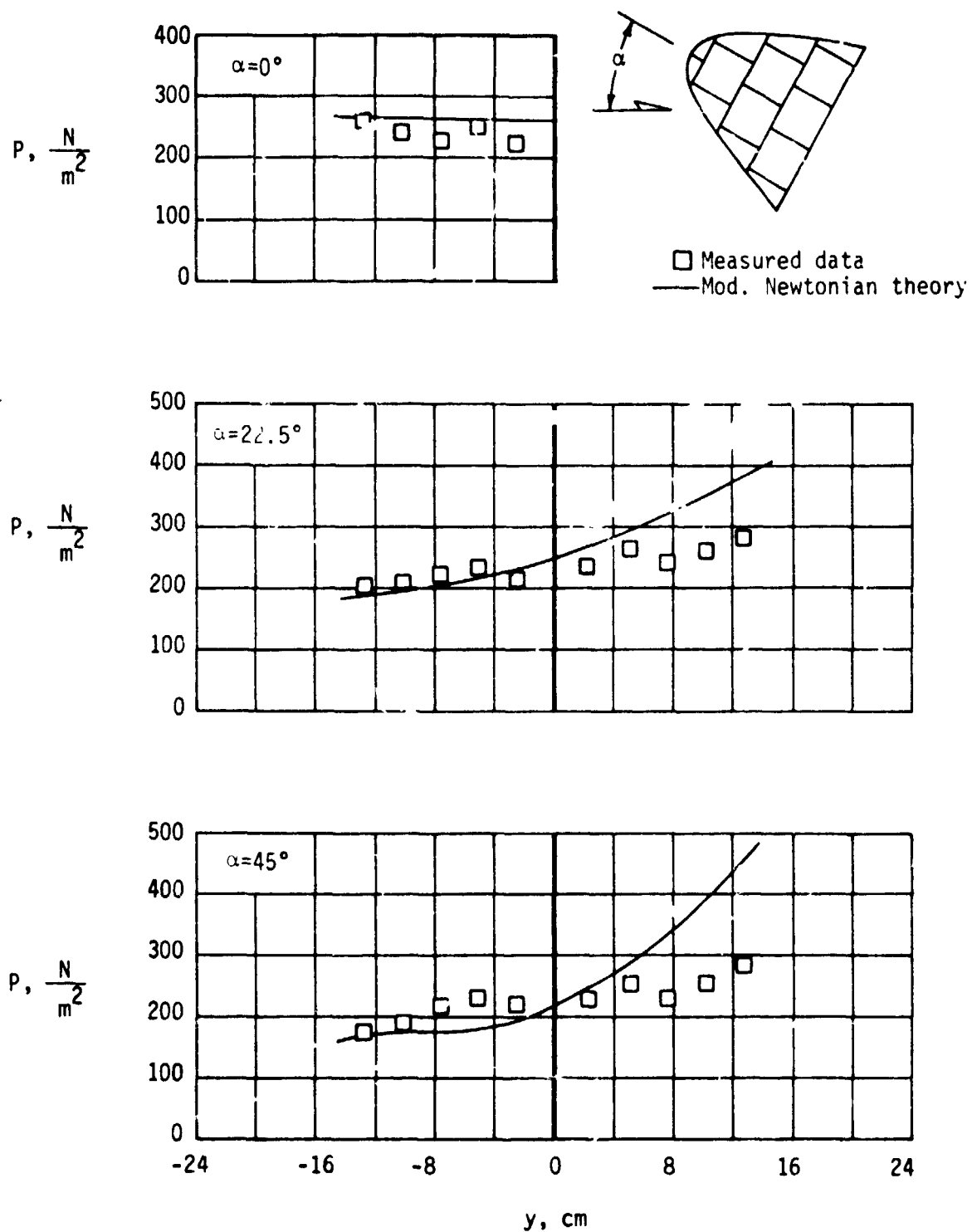


Figure 23.- Comparison of measured and modified Newtonian pressures₆ on the smoothed RSI tile array model. $Re_\infty/m = 3.3 \times 10^6$.

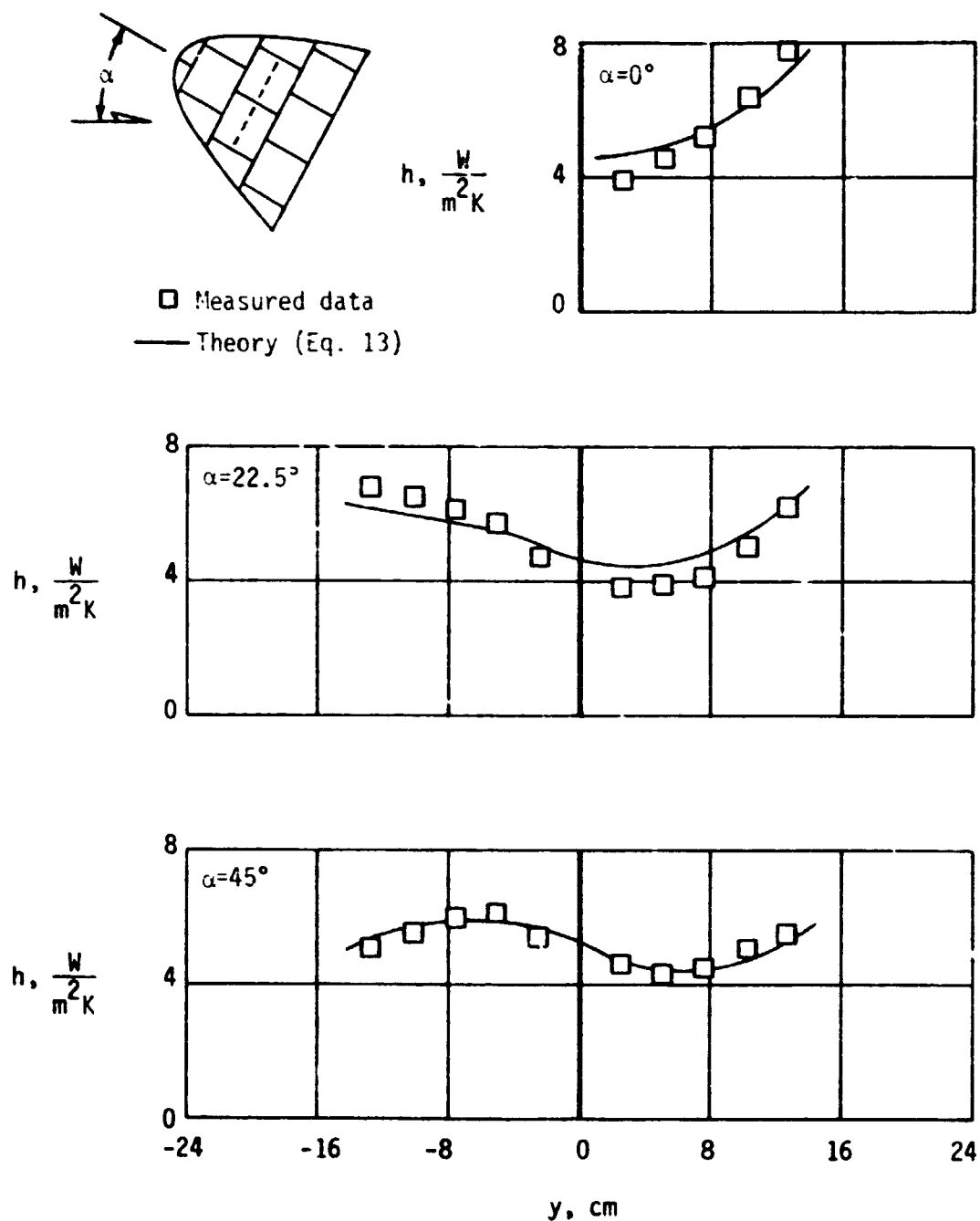


Figure 24.- Comparison of measured and predicted heat transfer to the smoothed RSI tile array model using measured pressure data. $Re_\infty/m = 3.3 \times 10^6$.

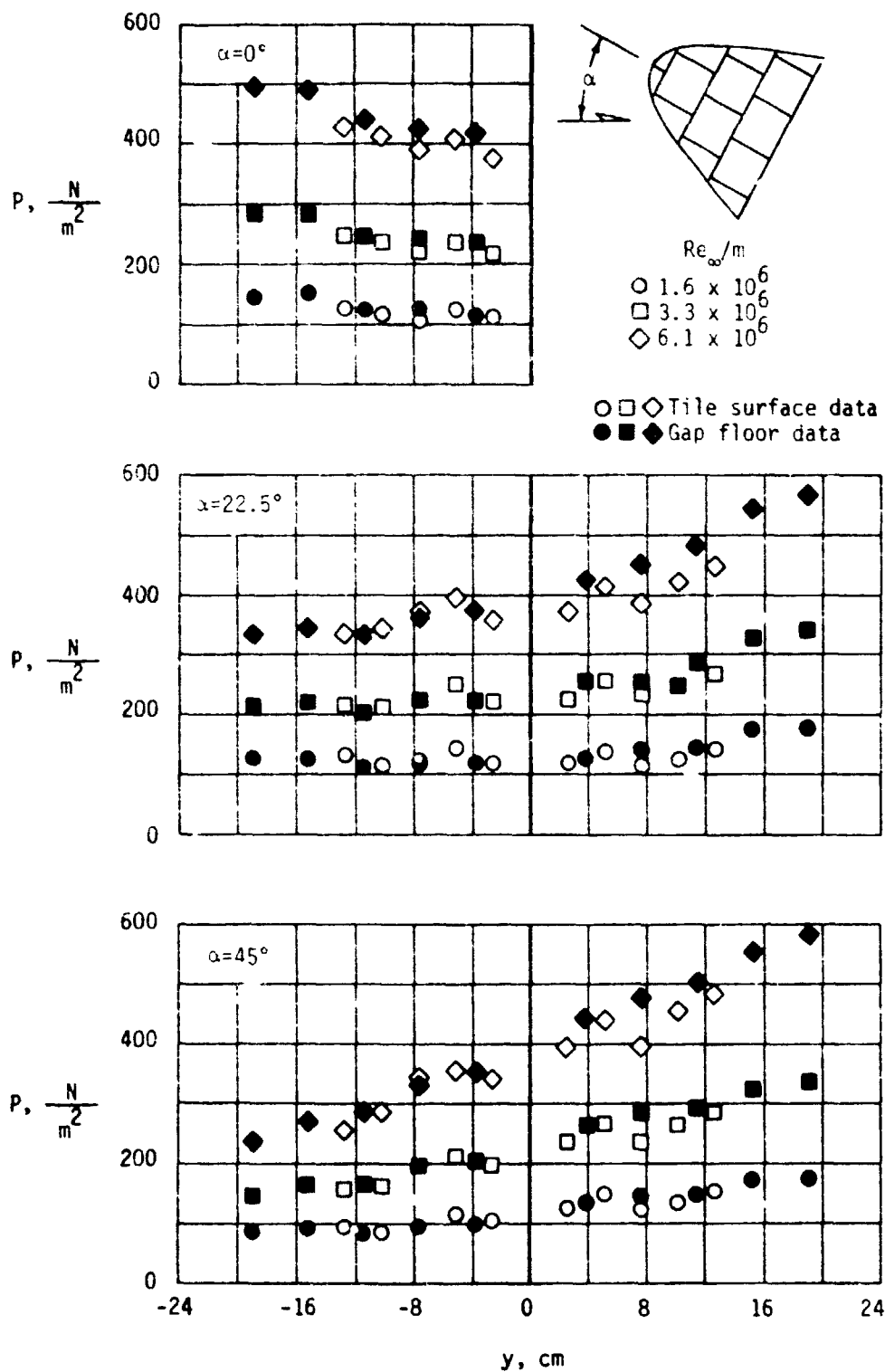
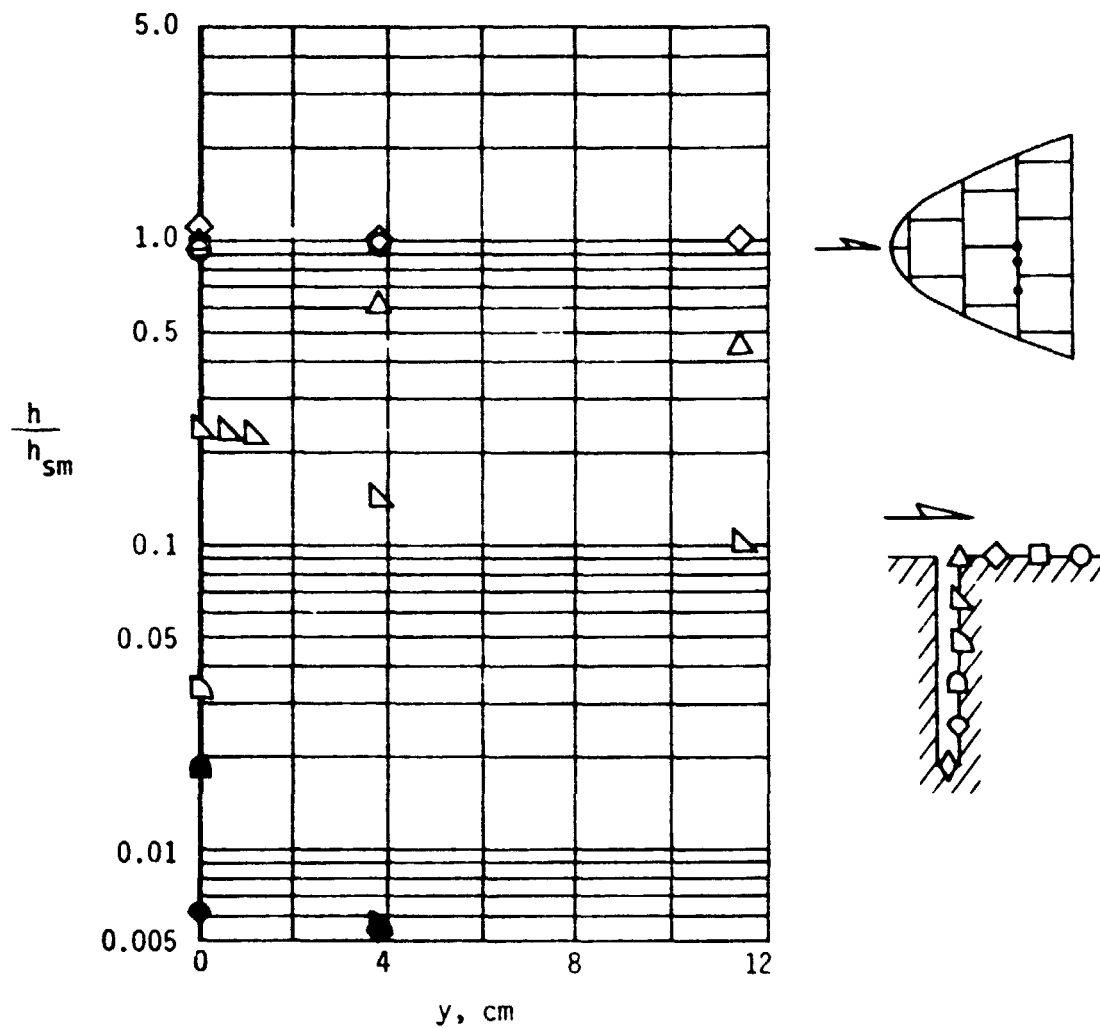
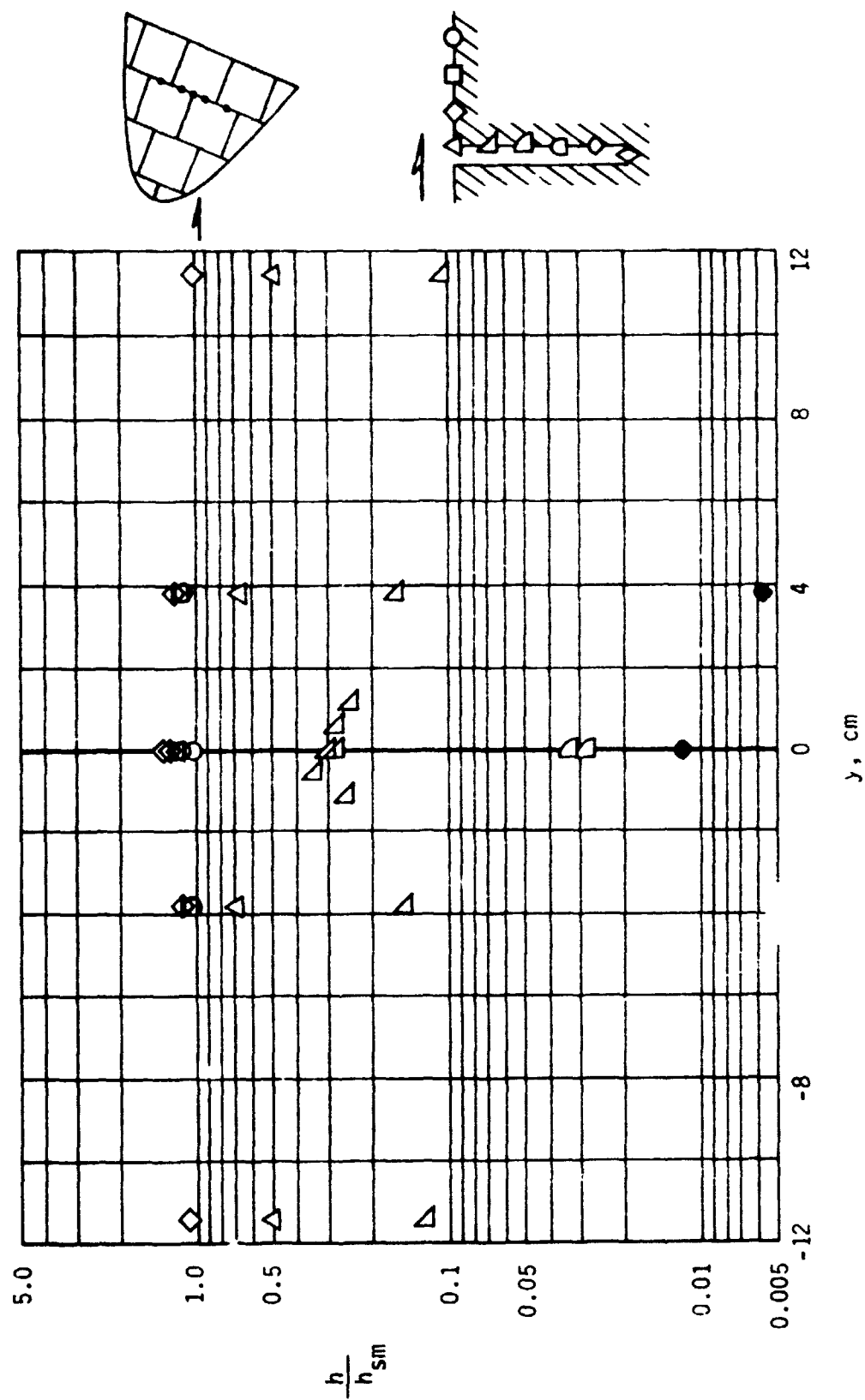


Figure 25.- Static pressure distributions on the RSI tile array model.



(a) $\alpha = 0^\circ$.

Figure 26.- Distribution of heat transfer within the transverse gap.
 $Re_\infty/m = 3.3 \times 10^6$.



(b) $\alpha = 22.5^\circ$.

Figure 26.- Continued.

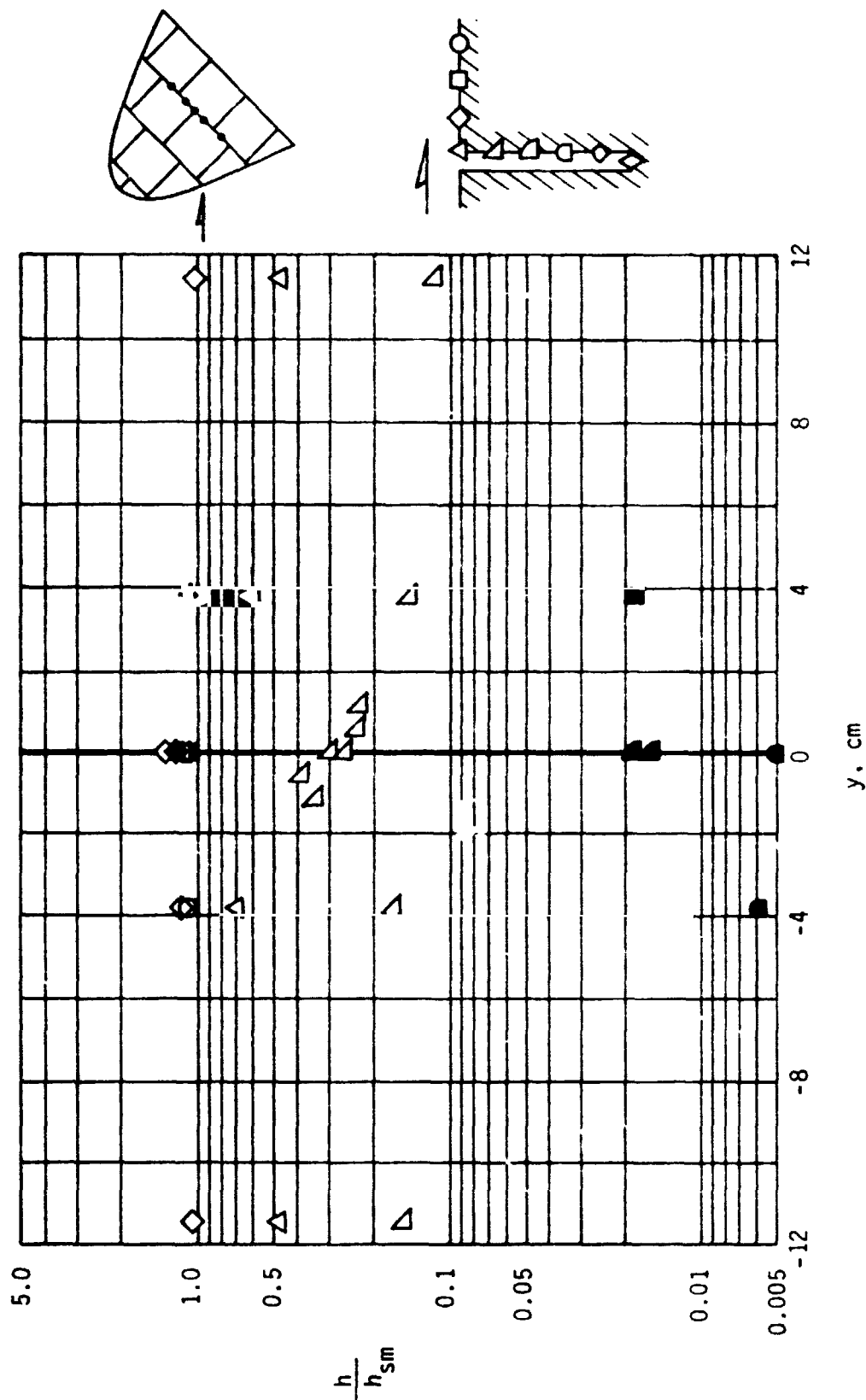
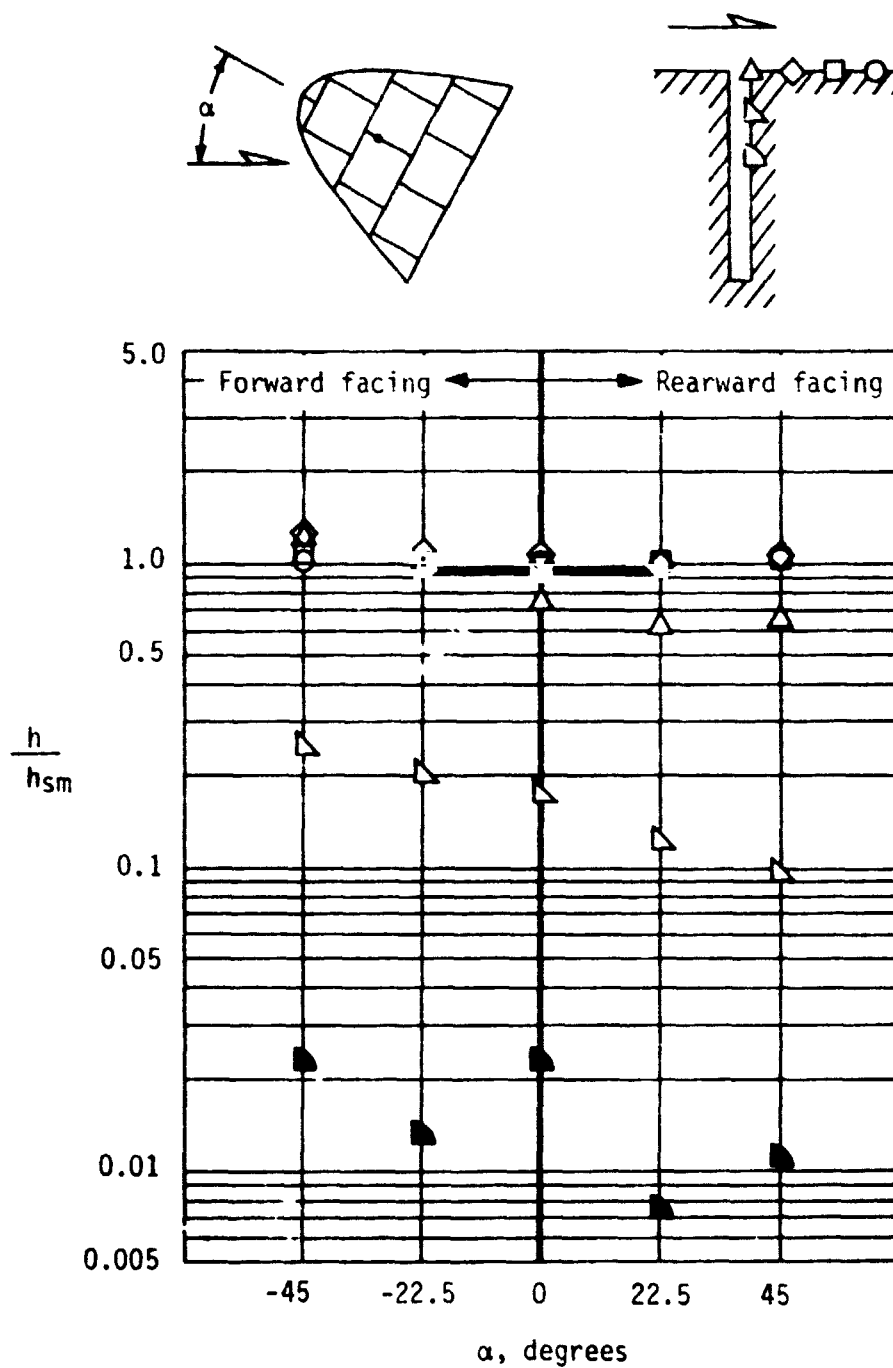
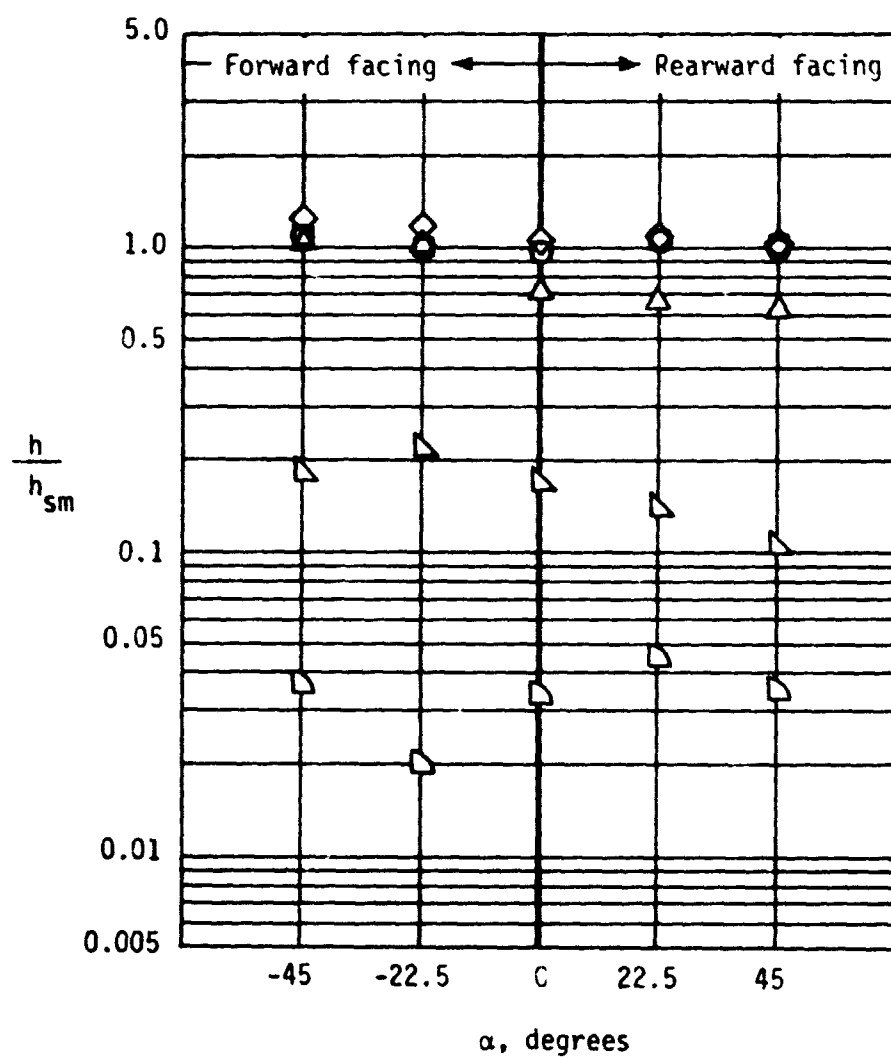
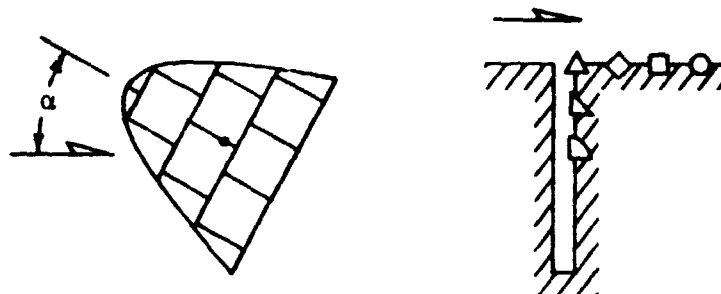
(c) $\alpha = 45^\circ$.

Figure 26.- Concluded.



(a) $x = -15.61$ cm.

Figure 27.- Variation of heat transfer to the streamwise gap with array rotation angle. $Re_{\infty}/m = 3.3 \times 10^6$.



(b) $x = -8.02$ cm.

Figure 27.- Concluded.

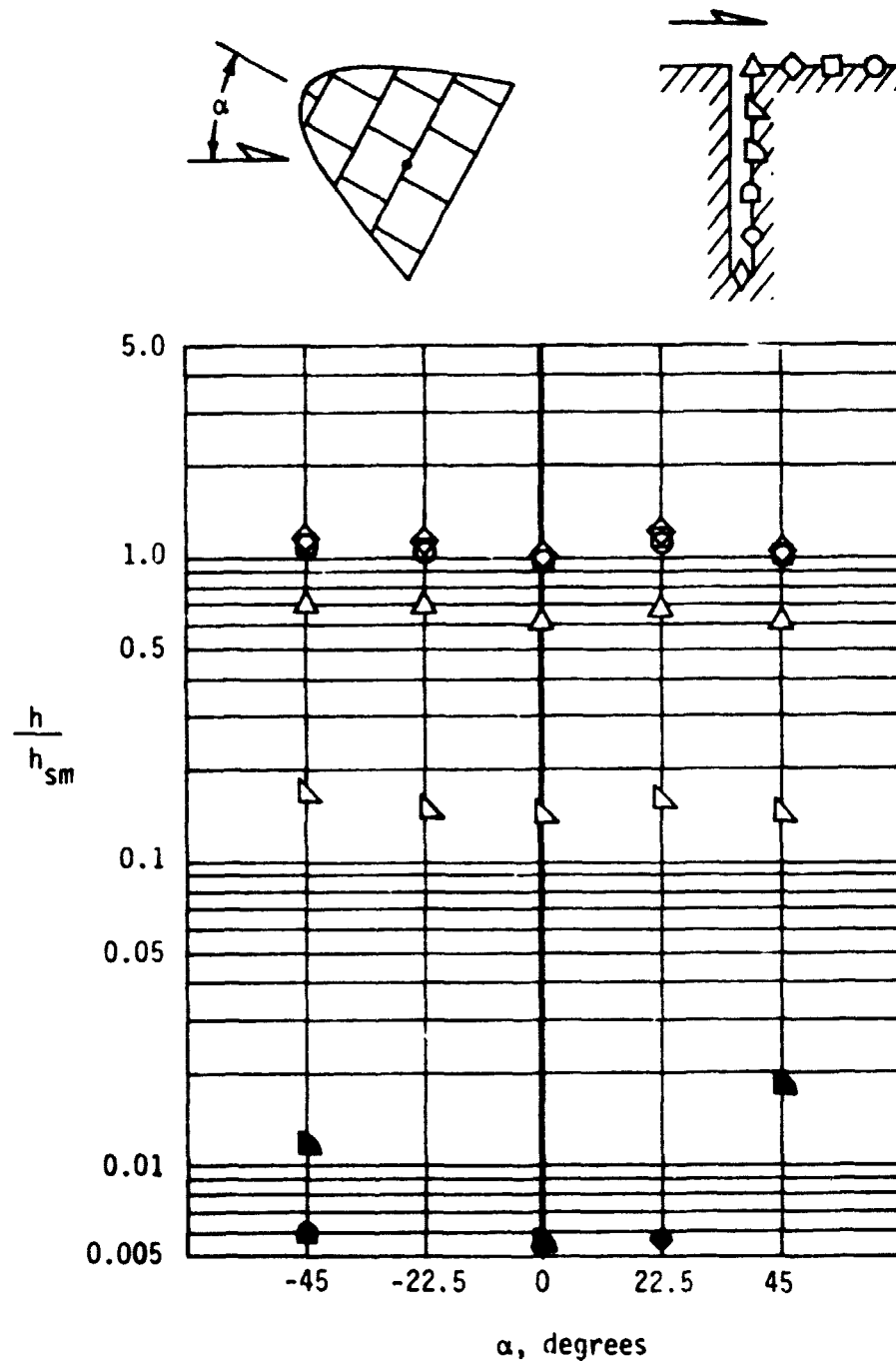


Figure 28.- Variation of heat transfer to the transverse gap with array rotation angle. $Re_{\infty}/m = 3.3 \times 10^6$

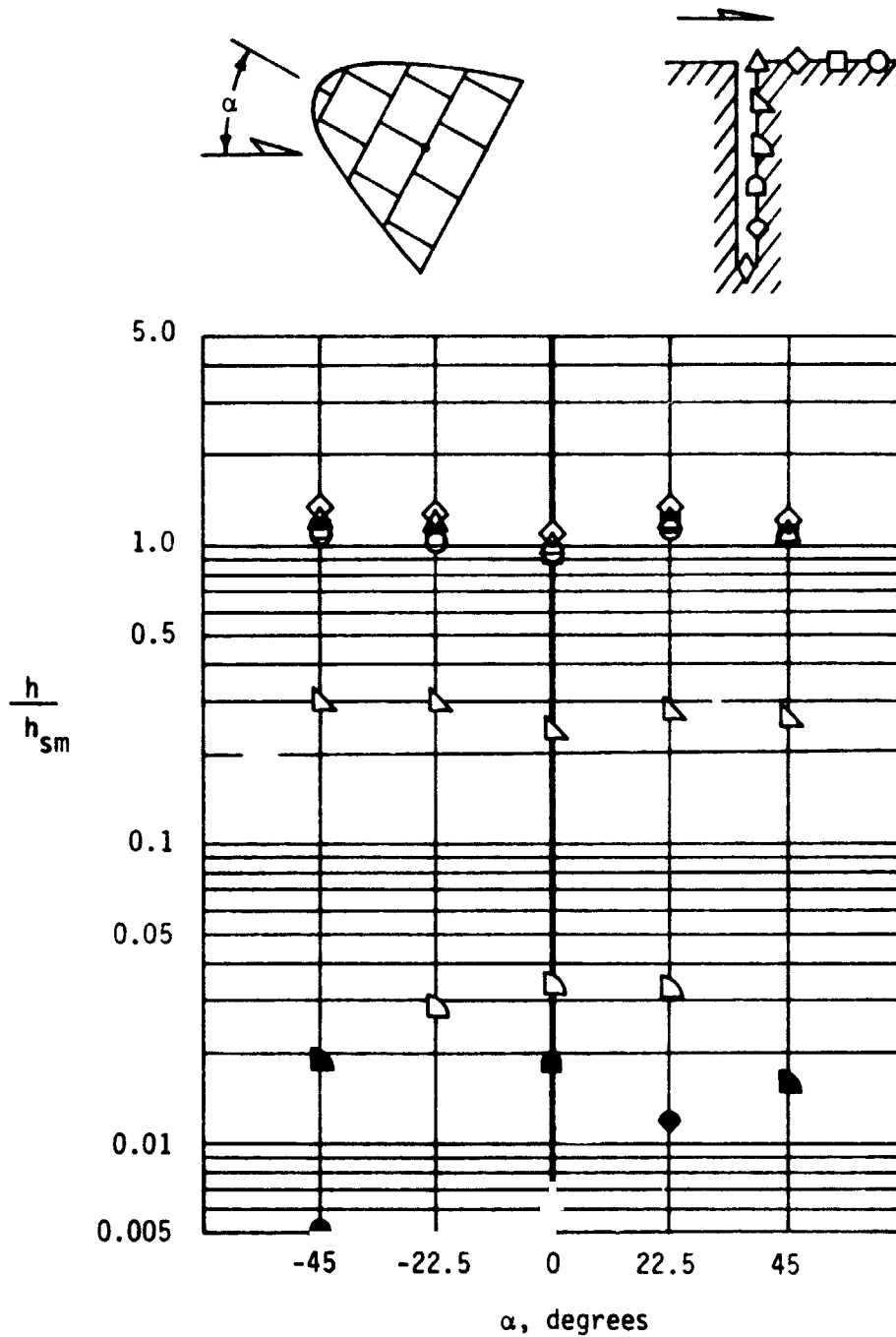


Figure 29.- Variation with array rotation angle of heat transfer to the transverse gap at its intersection with the streamwise gap. $Re_{\infty}/m = 3.3 \times 10^6$.

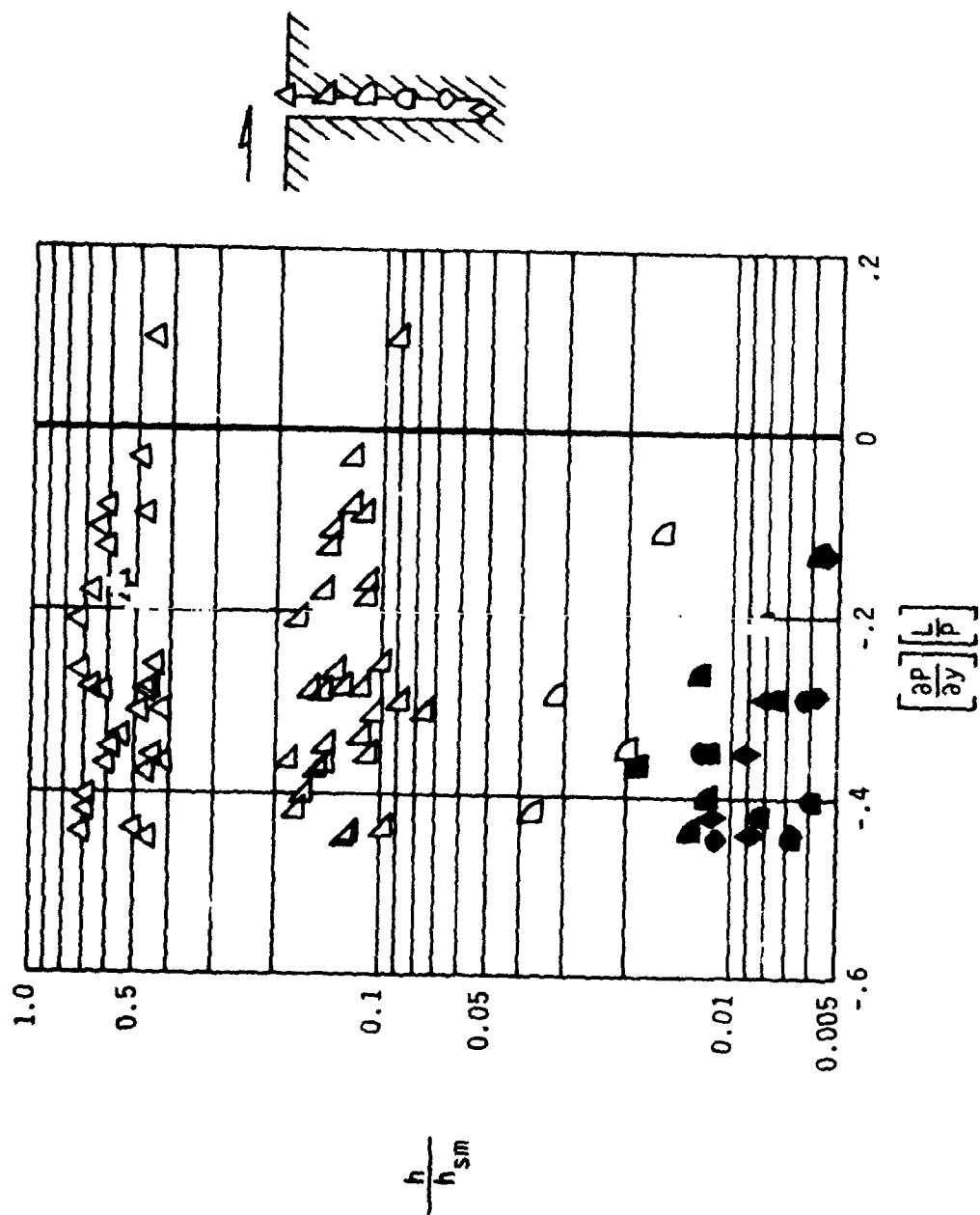


Figure 30.- Effect of pressure gradient on heat transfer to the transverse gap.

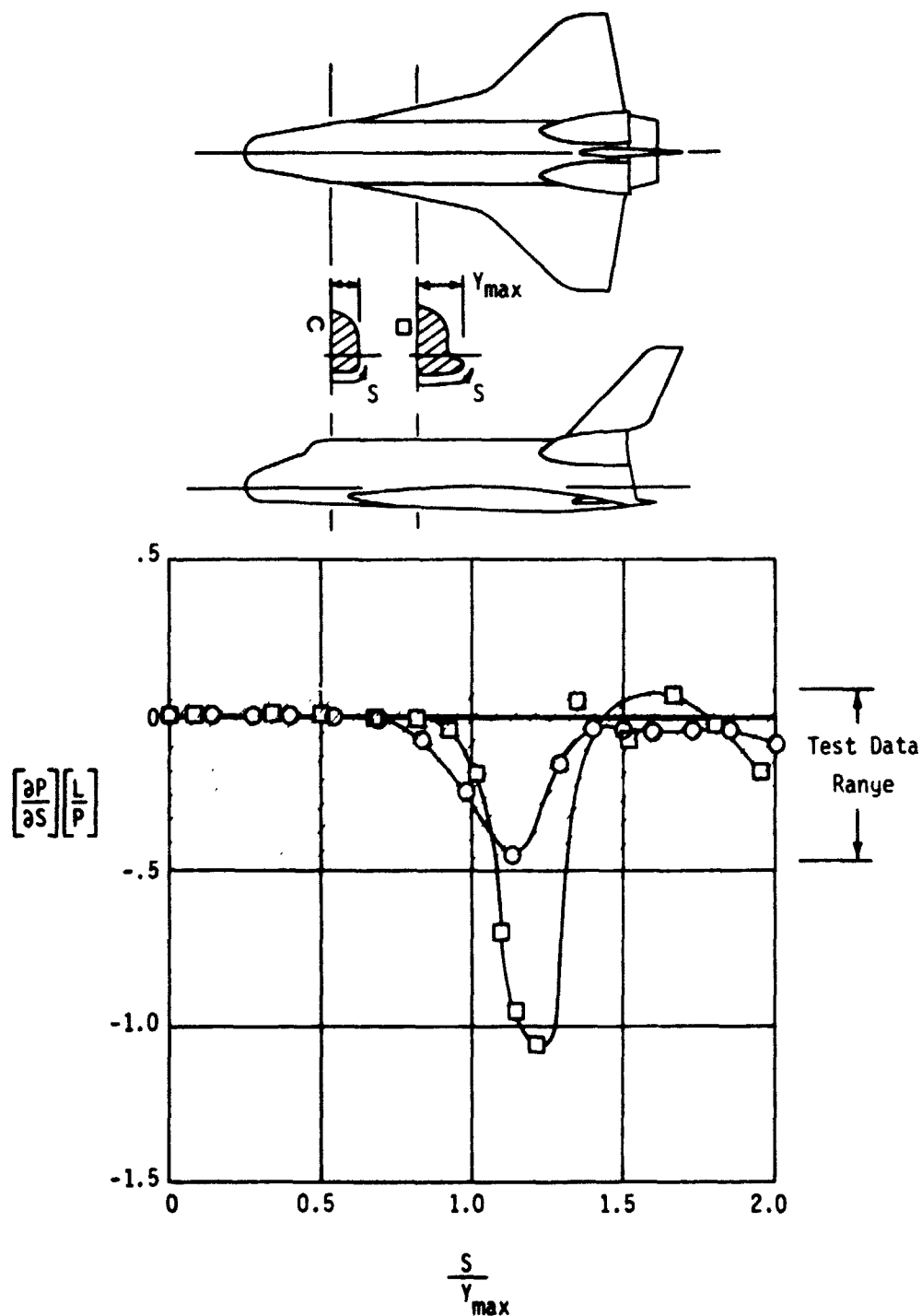


Figure 31.- Full scale vehicle pressure gradient simulation.
 $M_{\infty} = 10.0$, $\bar{\alpha} = 30^\circ$.

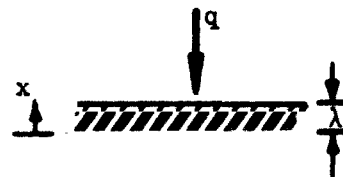
VIII. APPENDIX A

Heat Transfer Rate Measurement Technique

Aerodynamic heat transfer rate measurements were made using the thin-skin or transient-calorimeter technique. This technique uses the measured temperature response at the backface of a "thin" metallic model and the assumption that the model acts as a heat sink only with no front-to-backface temperature gradients (zero thickness) to compute model frontface heat transfer rates. Heat transfer rates computed by this method may be in error, however, because of the finite thickness of the model skin. The magnitude of this error may be assessed by comparing the solution for transient 1-dimensional heat conduction through a finite slab to the result for the "thin-skin" assumption.

Finite Thickness Slab

Consider the 1-dimensional transient conduction of heat through a finite solid of thickness λ , density ρ , specific heat c , and thermal conductivity k :



$$\frac{\partial T}{\partial t} = \kappa \frac{\partial^2 T}{\partial x^2} \quad (A-1)$$

$$\text{where } \kappa = \frac{k}{\rho c} \quad (A-2)$$

Initial condition:

$$T(x,0) = T_i \quad (A-3)$$

Boundary conditions:

$$k \frac{\partial T(0,t)}{\partial x} = 0 \quad (\text{Backface adiabatic}) \quad (A-4)$$

$$k \frac{\partial T(\lambda,t)}{\partial x} = q \quad \equiv \text{Constant} \quad (A-5)$$

The exact solution to this equation may be written (Ref. 30):

$$T(x,t) - T_i = \frac{2q\sqrt{\kappa t}}{k} \sum_{n=0}^{\infty} \left\{ \text{ierfc} \frac{(2n+1)\lambda - x}{2\sqrt{\kappa t}} + \text{ierfc} \frac{(2n+1)\lambda + x}{2\sqrt{\kappa t}} \right\} \quad (A-6)$$

$$\text{where } \text{ierfc } \eta \equiv \int_{\eta}^{\infty} \text{erfc } \xi \, d\xi$$

Solving for the backface temperature ($x = 0$):

$$T(0,t) - T_i = \frac{4q\sqrt{\kappa t}}{k} \sum_{n=0}^{\infty} \left\{ \text{ierfc} \frac{(2n+1)\lambda}{2\sqrt{\kappa t}} \right\} \quad (A-7)$$

Define

$$F_0 \equiv \frac{\kappa t}{\lambda^2}$$

then

$$T(0,t) - T_i = \frac{4q\lambda}{k} \sqrt{F_0} \sum_{n=0}^{\infty} \left\{ \text{ierfc} \frac{(2n+1)}{2\sqrt{F_0}} \right\} \quad (A-8)$$

Thin Skin Approximation

The "thin skin" approximation assumes an infinitely thin wall and therefore a simple energy balance between input heating rate and heat storage:

$$\rho c \lambda \frac{\partial T(t)}{\partial t} = q \quad \equiv \quad \text{constant} \quad (\text{A-9})$$

Initial condition:

$$T(0) = T_i \quad (\text{A-10})$$

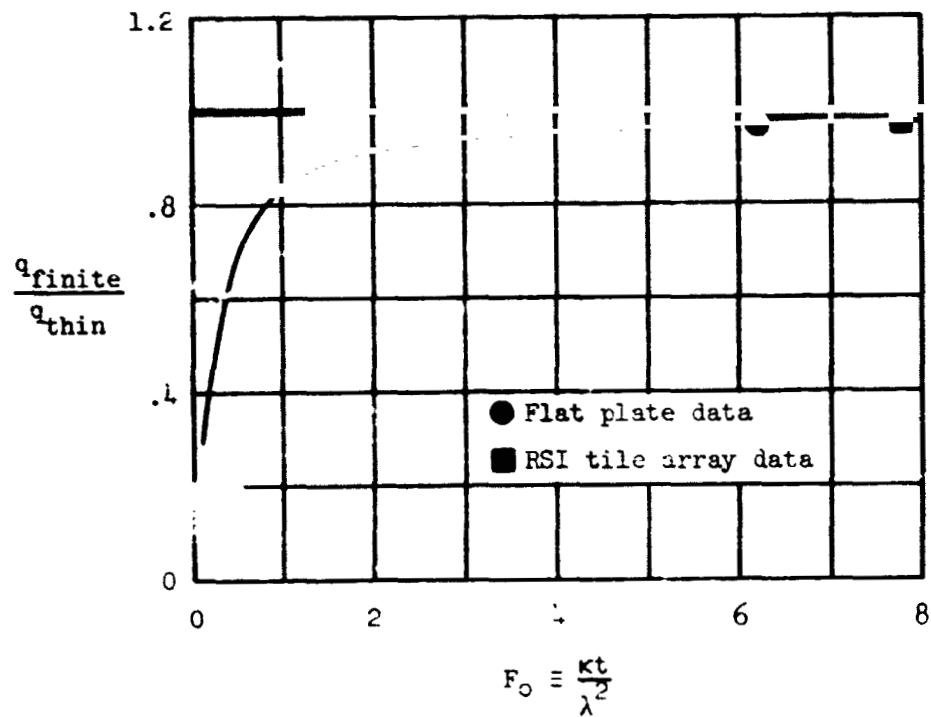
The solution is then:

$$T(t) - T_i = q \frac{t}{\rho c \lambda} \quad (\text{A-11})$$

or

$$T(t) - T_i = \frac{q \lambda}{k} F_0 \quad (\text{A-12})$$

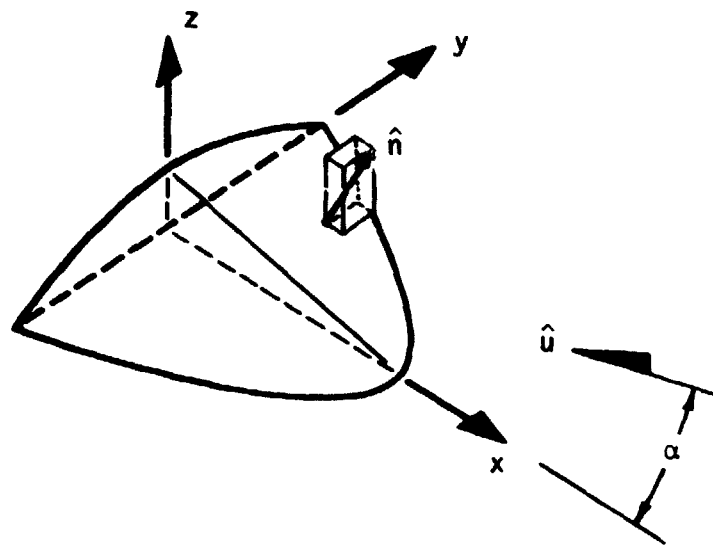
Comparison of equations (A-8) and (A-12) yields a direct relation for "thin-skin" versus finite-skin temperature response at the model skin backface. The ratio of actual finite-skin heating rate (q_{finite}) to "thin-skin" heating rate (q_{thin}) is a function only of the parameter $F_0 \equiv \frac{k t}{\lambda^2}$ and varies as shown in the following graph.



The error in measured heat transfer rates which results from the finite model skin thickness is less than 3.5 percent for both the flat plate and RSI tile array models.

IX. APPENDIX B

Surface Flow Deflection Angle



Consider the unit surface normal vector, \hat{n} :

$$\hat{n} = (\hat{n}_x, \hat{n}_y, \hat{n}_z) \quad (B-1)$$

and the unit freestream velocity vector, \hat{u} :

$$\hat{u} = (\hat{u}_x, \hat{u}_y, \hat{u}_z) \quad (B-2)$$

The scalar product of these vectors defines the angle between them,

$$\hat{n} \cdot \hat{u} = (\hat{n}_x \hat{u}_x + \hat{n}_y \hat{u}_y + \hat{n}_z \hat{u}_z) = \cos (90 + \phi) \quad (B-3)$$

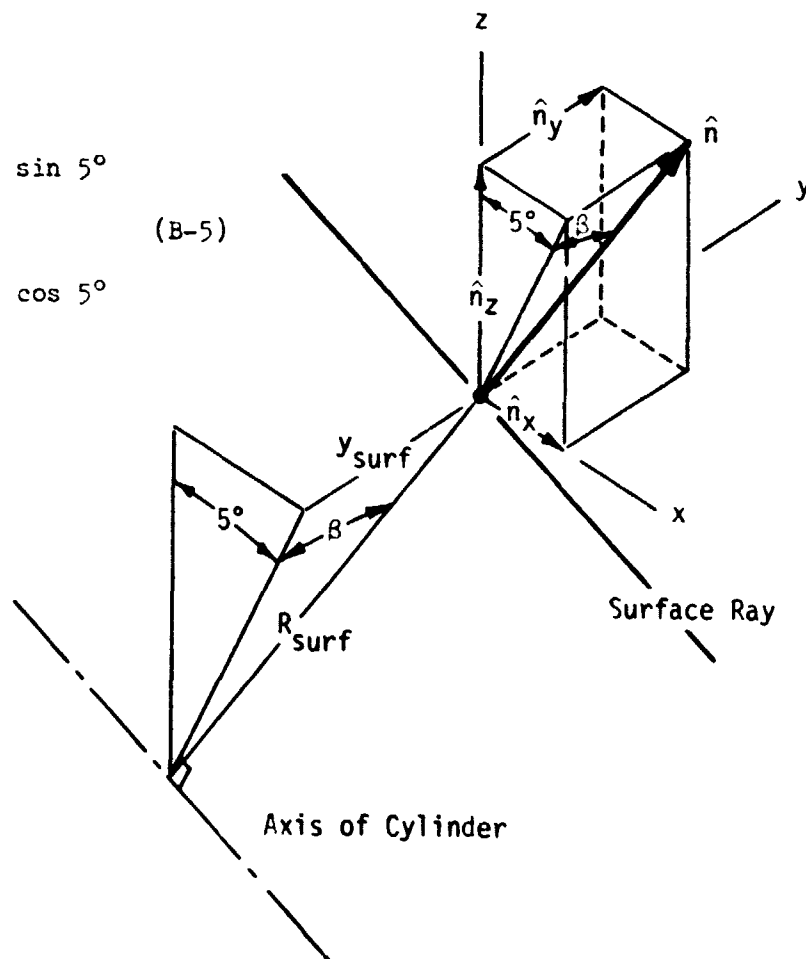
where $(90 + \phi)$ is the angle between the freestream velocity and surface normal vectors, and ϕ is the angle between the surface tangent plane and the freestream velocity vector.

Resolving unit vectors \hat{u} and \hat{n} into their component parts:

$$\begin{aligned}\hat{u}_x &= -\cos \alpha \\ \hat{u}_y &= -\sin \alpha \\ \hat{u}_z &= 0\end{aligned}\quad (B-4)$$

and

$$\begin{aligned}\hat{n}_x &= \cos \beta \sin 5^\circ \\ \hat{n}_y &= \sin \beta \\ \hat{n}_z &= \cos \beta \cos 5^\circ\end{aligned}\quad (B-5)$$



Substituting the components in (A-3):

$$\hat{n} \cdot \hat{u} = -\cos \beta \cos \alpha \sin 5^\circ - \sin \beta \sin \alpha = \cos (90 + \phi) \quad (\text{B-6})$$

But,

$$\sin \beta = \frac{y_{\text{surf}}}{R_{\text{surf}}} \text{ and } \cos \beta = \left(1 - \frac{y_{\text{surf}}^2}{R_{\text{surf}}^2}\right)^{\frac{1}{2}} \quad (\text{B-7})$$

Therefore,

$$\cos (90 + \phi) = - \left(1 - \frac{y_{\text{surf}}^2}{R_{\text{surf}}^2}\right)^{\frac{1}{2}} \cos \alpha \sin 5^\circ - \left(\frac{y_{\text{surf}}}{R_{\text{surf}}}\right) \sin \alpha \quad (\text{B-8})$$

or

$$\sin \phi = \left(1 - \frac{y_{\text{surf}}^2}{R_{\text{surf}}^2}\right)^{\frac{1}{2}} \cos \alpha \sin 5^\circ + \left(\frac{y_{\text{surf}}}{R_{\text{surf}}}\right) \sin \alpha \quad (\text{B-9})$$